Mon. Not. R. Astron. Soc. **296,** 119–149 (1998)

Stellar yields and chemical evolution – I. Abundance ratios and delayed mixing in the solar neighbourhood

D. Thomas,[1⋆] L. Greggio[1,2⋆] and R. Bender[1⋆]
[1]*Universitäts-Sternwarte München, Scheinerstr. 1, D-81679 München, Germany*
[2]*Dipartimento di Astronomia, Università di Bologna, I40100 Bologna, Italy*

Accepted 1997 October 30. Received 1997 October 13; in original form 1997 August 11

ABSTRACT

We analyse two recent computations of Type II supernova nucleosynthesis by Woosley & Weaver (hereafter WW95) and Thielemann, Nomoto & Hashimoto (hereafter TNH96), focusing on the ability to reproduce the observed [Mg/Fe] ratios in various galaxy types. We show that the yields of oxygen and total metallicity are in good agreement. However, TNH96 models produce more magnesium in the intermediate and less iron in the upper mass range of Type II supernovae than WW95 models. To investigate the significance of these discrepancies for chemical evolution, we calculate simple stellar population yields for both sets of models and different initial mass function slopes. We conclude that the Mg yields of WW95 do not suffice to explain the [Mg/Fe] overabundance either in giant elliptical galaxies and bulges or in metal-poor stars in the solar neighbourhood and the Galactic halo. Calculating the chemical evolution in the solar neighbourhood according to the standard infall model, we find that, using WW95 and TNH96 nucleosynthesis, the solar magnesium abundance is underestimated by 29 and 7 per cent, respectively.

We include the relaxation of the instantaneous mixing approximation in chemical evolution models by splitting the gas component into two different phases. In additional simulations of the chemical evolution in the solar neighbourhood, we discuss various time-scales for the mixing of the stellar ejecta with the interstellar medium. We find that a delay of the order of 10^8 yr leads to a better fit of the observational data in the [Mg/Fe]–[Fe/H] diagram without destroying the agreement with solar element abundances and the age–metallicity relation.

Key words: supernovae: general – Galaxy: halo – solar neighbourhood – Galaxy: stellar content – galaxies: abundances – galaxies: stellar content.

1 INTRODUCTION

Understanding the formation and evolution of galaxies is difficult because it involves many different processes that are coupled in a complex way. In order to simulate a scenario properly, one has to consider the dynamics of stars, gas and dark matter as well as star formation, the interaction with the interstellar medium (ISM), and chemical enrichment (Hensler & Burkert 1990). Since this problem includes many unknown parameters, it is more effective to decouple various processes and to inspect closely observational constraints that are relevant to the different parameters.

Chemical evolution models constrain star formation histories, supernova rates and abundances in the ISM, in the stars, and in the intracluster medium (ICM). Thus trying to reproduce element abundances in chemical simulations already puts significant constraints on galaxy formation without considering complicated dynamical aspects. Hence, at the present stage it is more effective to decouple the dynamical and the chemical approaches.

Different time-scales for the duration of the star-forming phase cause different abundance ratios in the stars and in the ISM. In short phases of star formation short-living, massive stars govern the enrichment of the ISM. Thus in those formation scenarios the abundance ratios reflect the Type II supernova (SN II) production (Hashimoto, Iwamoto & Nomoto 1993a).

In order to obtain the various element abundances in the solar neighbourhood, a modest and continuous star formation rate (SFR) is necessary (Matteucci et al. 1989). In the standard models (e.g. Matteucci & Greggio 1986; Timmes, Woosley & Weaver 1995; Tsujimoto et al. 1995), this kind of star formation history is obtained with infall of primordial gas on a time-scale of several Gyr and an SFR that depends on the gas density via the Schmidt law (Schmidt 1959, 1963). In this scenario, the disc of the Galaxy is assumed to form out of slowly accreting gas. Since star formation occurs over a long time-scale of 10^{10} yr, the chemical evolution is noticeably influenced by Type Ia supernovae (SNe Ia).

⋆E-mail: daniel@usm.uni-muenchen.de (DT); greggio@usm.uni-muenchen.de (LG); bender@usm.uni-muenchen.de (RB)

In bulges and elliptical galaxies, [α/Fe] ratios seem to be enhanced with respect to solar abundances (Peletier 1989; Worthey, Faber & Gonzalez 1992; Davies, Sadler & Peletier 1993; McWilliam & Rich 1994). Since the α-elements are mainly produced in massive stars experiencing SN II explosions (Woosley 1986), and iron is substantially contributed by SNe Ia, the chemical history of the light-dominating component of the stellar population in bulges and ellipticals must be dominated by massive stars. In chemical evolution models, this can be realized by (Worthey et al. 1992; Matteucci 1994)

(i) a flat IMF, or
(ii) a short phase of star formation, or
(iii) a low fraction of close binary systems experiencing SNe Ia.

Chemical evolution models have to constrain and quantify these different possibilities.

Although in the pure chemical approach the number of input parameters is already reduced, there are still plenty of uncertainties in the calculations. Typical input parameters are the shape and slope of the initial mass function (IMF), the SFR, the infall rate and the fraction of close binary systems producing iron via SNe Ia. However, chemical evolution is also very sensitive to the adopted stellar yields, especially of SNe II (see also Gibson 1997). Thus, besides the parameters above, chemical evolution models should always take into account different stellar nucleosynthesis prescriptions, which are strongly affected by uncertainties of stellar evolution models (Thielemann et al. 1996).

In this paper, we compare two recently published nucleosynthesis calculations for SNe II by

(i) Woosley & Weaver (1995), hereafter WW95, and
(ii) Thielemann et al. (1996) and Nomoto et al. (1997),[1] hereafter TNH96.

We focus on the question of whether the considered sets of models are able to explain an important observed feature of galaxy formation: the [Mg/Fe] overabundance. There is a broad consensus that metal-poor halo stars in our Galaxy have magnesium-enhanced abundance ratios (Gratton & Sneden 1988; Magain 1989; Edvardsson et al. 1993; Axer, Fuhrmann & Gehren 1994, 1995; Fuhrmann, Axer & Gehren 1995). The exact value of the enhancement is still debatable, but it seems to converge to $0.3 - 0.4$ dex (Truran & Burkert 1993; Gehren 1995). This observation can be easily understood by taking into account that metal-poor stars form in the early stages of the galaxy formation, when the enrichment due to SNe II is dominating chemical evolution. However, we will show that there are still unresolved problems caused by uncertainties in stellar nucleosynthesis.

As already noted, in elliptical galaxies there are strong indications from spectra in the visual light that there is a magnesium overabundance of at least 0.2 dex in nuclei of these galaxies (Worthey et al. 1992; Weiss, Peletier & Matteucci 1995). However, while the halo in the solar neighbourhood has low metallicities ($-3 \leq$[Fe/H]≤ -1), the stars that dominate the visual light in the nuclei of ellipticals have solar or super-solar Z (Greggio 1997). Therefore, the [Mg/Fe] overabundance is realized at both low and high Z in two considerably different systems. While a detailed inspection of element abundances in elliptical galaxies will be the subject of a forthcoming paper, in this work we concentrate on the chemical evolution of the solar neighbourhood using WW95 and TNH96 SN II yields.

[1] In this paper, the results of Thielemann et al. (1996) are extended on a larger mass range.

In order to calibrate our code, we use the same approach as in the most common chemical evolution models (Matteucci & Greggio 1986; Timmes et al. 1995) for the solar neighbourhood, performing the calculation for both sets of nucleosynthesis prescriptions. Taking finite stellar lifetimes into account, the classical numerical models relax the instantaneous recycling approximation, but usually assume the stellar ejecta to mix instantaneously with the ISM (Tinsley 1980). Only few attempts have been made in the literature to relax the instantaneous mixing approximation in numerical models of chemical evolution (see discussion in Timmes et al. 1995). We present a modification of the basic equations (Tinsley 1980) splitting the gaseous mass into two different phases, one including the stellar ejecta and the second being cool and well mixed. The mixing process is characterized by a gas flow from the first, inactive to the active, star-forming gas phase. We additionally present the results of simulations considering this modification.

In Section 2 we summarize the most important aspects of chemical evolution, while in Section 3 we discuss stellar yields from SN II explosions, comparing WW95 and TNH96. We analyse their influence on chemical evolution by calculating the SSP yields of various elements in Section 4. In Section 5 we present our model for the chemical evolution in the solar neighbourhood. In our conclusions we summarize the main results.

2 GENERALITIES ON CHEMICAL EVOLUTION

2.1 The basic equations

Non-primordial elements develop in a cycle of birth and death of stars. These form out of the ISM, process elements, and eject them during the late stages of their evolution in the form of stellar winds, planetary nebulae (PNe), or supernovae (SNe Ia and SNe II), depending on their main-sequence mass m. The formation of stars and the re-ejection of gas can be described by the following phenomenological equations (Tinsley 1980):

$$\mathrm{d}M_{\mathrm{tot}}/\mathrm{d}t = f, \tag{1}$$

$$\mathrm{d}M_{\mathrm{s}}/\mathrm{d}t = \psi - E, \tag{2}$$

$$\mathrm{d}M_{\mathrm{g}}/\mathrm{d}t = -\psi + E + f. \tag{3}$$

The total baryonic mass $M_{\mathrm{tot}} = M_{\mathrm{s}} + M_{\mathrm{g}}$ is governed by infall or outflow f of material, being either primordial or enriched gas. The total stellar mass M_{s} is *increasing* according to the SFR ψ and *decreasing* due to re-ejection E of gas. The total gaseous mass M_{g} behaves exactly contrary to M_{s} with the additional component of infalling or outflowing gas f.

The ejection rate E is obtained by integrating the ejected mass fraction $(1 - w_m)$, folded with the SFR and the normalized IMF ϕ, from the turn-off mass m_{t} to the maximum stellar mass m_{max}. Here, w_m denotes the mass fraction of the remnant.

$$E(t) = \int_{m_{\mathrm{t}}}^{m_{\mathrm{max}}} (1 - w_m)\, \psi(t - \tau_m)\, \phi(m)\, \mathrm{d}m. \tag{4}$$

The quantity τ_m is the stellar lifetime of a star with mass m. In the instantaneous recycling approximation, τ_m is assumed to be negligible in comparison with the time t. This approximation is relaxed in numerical simulations as well as in our evolution code. This must not be confused with the instantaneous mixing approximation (IMA) which is assumed in most chemical evolution models (Matteucci & Greggio 1986; Timmes et al. 1995; Tsujimoto et al. 1995; Pagel & Tautvaisiene 1995). In Section 5, we also relax this

assumption and take a delay in the mixing of the stellar ejecta into account.

Parallel to equation (3), the mass production of the element i in the ISM ($X_i M_g$) is expressed in the equation below:

$$\mathrm{d}(X_i M_g)/\mathrm{d}t = -X_i\,\psi + E_i + X_{i,f} f. \tag{5}$$

Here, X_i is the abundance of element i in the ISM; $X_{i,f}$ is the abundance of element i in the infalling or outflowing gas. The element ejection rate E_i is obtained by integrating the ejected mass fraction Q_{im} (including both initial abundance and newly produced material) of the element i, again folded with the SFR and IMF over the appropriate mass range, equivalently to equation (4):

$$E_i(t) = \int_{m_t}^{m_{\max}} Q_{im}\;\psi(t-\tau_m)\,\phi(m)\;\mathrm{d}m. \tag{6}$$

Equations (3) and (5) can be combined to describe the progression of the abundance X_i of element i in the ISM:

$$M_g\,\mathrm{d}X_i/\mathrm{d}t = E_i - X_i\,E + (X_{i,f} - X_i)f. \tag{7}$$

The key value in this equation is the stellar yield Q_{im} hidden in the element ejection rate E_i.We neglect stellar winds during the evolution, and assume that the stars enrich the ISM at the time when they die. Depending on their initial mass, they either experience an SN II explosion ($m > 8\,\mathrm{M}_\odot$) or become a white dwarf blowing off their envelopes ($m < 8\,\mathrm{M}_\odot$). Elements heavier than oxygen are mainly processed in supernovae. A substantial fraction of iron is contributed by SNe Ia. Adopting the description of the supernova rates from Greggio & Renzini (1983), the element ejection rate integrated over the total mass range can be described with the following equation as in Matteucci & Greggio (1986) and Timmes et al. (1995),

$$\begin{aligned} E_i(t) = & \int_{16}^{m_{\max}} Q_{im}^{\mathrm{SNII}}\psi(t-\tau_m)\phi(m)\mathrm{d}m \\ & + (1-A)\int_8^{16} Q_{im}^{\mathrm{SNII}}\psi(t-\tau_m)\phi(m)\mathrm{d}m \\ & + (1-A)\int_3^{8} Q_{im}^{\mathrm{PN}}\psi(t-\tau_m)\phi(m)\mathrm{d}m \\ & + A\int_3^{16}\phi(m)\,\mathrm{d}m\int_{\mu_{\inf}}^{0.5} 24\mu^2 Q_{im}^{\mathrm{SNIa}}\psi(t-\tau_{\mu m})\,\mathrm{d}\mu \\ & + \int_1^3 Q_{im}^{\mathrm{PN}}\psi(t-\tau_m)\phi(m)\mathrm{d}m. \end{aligned} \tag{8}$$

In this equation, the enrichment due to stars in the mass range $3-16\,\mathrm{M}_\odot$ is split into a contribution by Type II supernovae (Q^{SNII}) plus planetary nebulae (Q^{PN}), due to single stars, and Type Ia supernovae (Q^{SNIa}), assumed to be the end product of close binary evolution. In the formulation of Greggio & Renzini (1983), μ is the ratio between the mass of the secondary and the total mass m of the system. The maximum fraction of the secondary is 0.5 by definition, while the minimum mass $\mu_{\inf}$ is dependent on the turn-off as defined in the following equation (Greggio & Renzini 1983):

$$\mu_{\inf} \equiv \max\,[m_t/m, (m-8)/m]. \tag{9}$$

One has to integrate the distribution of the secondary component $f(\mu) \sim \mu^2$, folded with the yield (independent of the mass of the system) and the SFR over the appropriate mass range. The clock of the SN Ia explosion is given by the lifetime of the secondary $\tau_{\mu m}$, the mass of which can be as low as $0.8\,\mathrm{M}_\odot$ (Greggio & Renzini 1983). Thus, the enrichment due to SNe Ia is substantially delayed with respect to SNe II. The degree of influence by SNe Ia highly depends on the fraction A of close binaries, which is a free parameter in chemical evolution. Greggio & Renzini (1983) calibrate A on the ratio between the current Type II and Type Ia supernova rates in the Galaxy.

It should be noticed that equation (8) is not completely consistent, since m refers to the mass of single and binary stars. Nevertheless, as long as the parameter A is small (as in our case), Type Ia events can be regarded as a small perturbation. Hence, equation (8) is an acceptable approximation, and it allows us to describe the delayed release of iron from SNe Ia.

In these terms, the rates of Type II and Ia supernovae can be described by the following equations:

$$R_{\mathrm{II}} = \int_{16}^{m_{\max}} \psi(t-\tau_m)\frac{\phi(m)}{m}\mathrm{d}m + (1-A)\int_8^{16}\psi(t-\tau_m)\frac{\phi(m)}{m}\mathrm{d}m, \tag{10}$$

$$R_{\mathrm{Ia}} = A\int_3^{16}\frac{\phi(m)}{m}\,\mathrm{d}m\int_{\mu_{\inf}}^{0.5} 24\mu^2\psi(t-\tau_{\mu m})\,\mathrm{d}\mu. \tag{11}$$

2.2 Parameter constraints

In spite of the several unknown parameters (IMF slope x, SFR as a function of time, stellar yields), the following arguments show how they can be constrained by different observational information, step by step. This is useful for the interpretation of the results from chemical evolution calculations.

Assuming the instantaneous recycling approximation, one can take ψ out of the integral in equation (4). For large t, the residual integral expressing the returned fraction R_x depends strongly on the IMF slope x but only marginally on turn-off mass (and then time). Equation (2) can then be written as

$$\mathrm{d}M_s/\mathrm{d}t \approx \psi(1-R_x). \tag{12}$$

The integrated solution demonstrates that the final total mass of stars depends on the *time-averaged* star formation rate $\bar{\psi}$ and the IMF slope:

$$M_s \approx M_{s,0} + (1-R_x)\int_{t_0}^{t}\psi(t')\mathrm{d}t', \tag{13}$$

where the subscript zero refers to the initial conditions. Similar considerations show that the final mass of gas in the ISM depends on a mean SFR $\bar{\psi}$, a mean infall rate $\bar{f}$ and the IMF slope:

$$M_g \approx M_{g,0} - (1-R_x)\int_{t_0}^{t}\psi(t')\mathrm{d}t' + \int_{t_0}^{t} f(t')\mathrm{d}t'. \tag{14}$$

Now we need an approximation to pin down x. For this purpose, we consider the element abundances at the time t. The above approximation applied to equation (5) leads to

$$\begin{aligned} X_i M_g \approx & X_{i,0}M_{g,0} - (X_i - X_{i,0})\bar{\psi}(t-t_0) \\ & + R_{ix}\bar{\psi}(t-t_0) + \left(X_{i,f} - X_{i,f,0}\right)\bar{f}(t-t_0), \end{aligned} \tag{15}$$

with R_{ix} as the returned mass fraction of element i mostly dependent on the IMF slope and the stellar yield. If we consider an element the stellar yield of which is well known, we get a constraint on x (with known abundance of the infalling gas), for a given minimum mass $m_{\min}$ of the stellar population.

To summarize, the stellar and gaseous masses at the current epoch and the abundance of a specific element with relatively certain yield constrain $\bar{\psi}$,$\bar{f}$ and x. We can then draw conclusions on the nucleosynthesis of other elements, the stellar yields of which are relatively uncertain. In other words, from chemical evolution of galaxies one can get a constraint on the stellar evolution models.

This is a convincing example of how tightly these two disciplines are coupled. Since the approximation $\tau_m \ll t$ is especially valid for elements produced mainly by SNe II, we will use this strategy in Section 5 to fix the IMF slope with the element oxygen and constrain the necessary magnesium yield in SNe II.

2.3 The initial mass function

The IMF is as usual assumed to be a declining function of mass, according to a power law: $\phi \sim m^{-x}$. Since the IMF is usually normalized *by mass*, the actual amount of mass created in one generation of stars is controlled by the SFR ψ:

$$\int_{m_{\rm min}}^{m_{\rm max}} \phi(m) {\rm d}m = 1. \quad (16)$$

In these terms, the slope $x = 1.35$ corresponds to the Salpeter value (Salpeter 1955).

To avoid uncertain extrapolations of the stellar yields to the high-mass end, we have adopted $m_{\rm max} = 40\,{\rm M}_\odot$ which is the maximum mass for which WW95 models are computed. TNH96 do give the yields for a 70-$M_\odot$ star. For the comparison between the two sets of models we keep $m_{\rm max}$ fixed at $40\,{\rm M}_\odot$. The effect of adopting $m_{\rm max} = 70\,{\rm M}_\odot$ is explored in Sections 4.5 and 5.3.

The lower cut-off of one generation of stars is assumed to be $m_{\rm min} = 0.1\,{\rm M}_\odot$. The higher the minimum mass, the larger the fraction of massive stars, thus more metals are produced. Abundance ratios, however, are not affected by the choice of $m_{\rm min}$.

Alternative formulations of the IMF with different slopes at different mass ranges exist in the literature (e.g. Scalo 1986; Kroupa, Tout & Gilmore 1993; Gould, Bahcall & Flynn 1997). However, in order to keep the number of free parameters low, we have decided to fix $m_{\rm min} = 0.1\,{\rm M}_\odot$ and use one specific slope x for the whole mass range. The value of x, instead, is treated as a free parameter.

3 STELLAR YIELDS AND NUCLEOSYNTHESIS

3.1 PNe and SNe Ia

In our calculations, we use the results in Renzini & Voli (1981) for the enrichment due to intermediate-mass single stars ($1 \le m \le 8\,{\rm M}_\odot$). In particular we select the models with $\alpha = 1.5$, $\eta = 0.33$.

SNe Ia are assumed to occur in close binary systems (Whelan & Iben 1973). In this model, the explosion is caused by a carbon deflagration of the material-accreting degenerate white dwarf (Hansen & Wheeler 1969; Nomoto 1980a,b; Weaver & Woosley 1980; Nomoto 1981). We adopt the results of the nucleosynthesis from the classical W7 model by Nomoto, Thielemann & Yokoi (1984).

Low-mass stars, in the range 1 to $8\,{\rm M}_\odot$, do not contribute to the enrichment of O, Mg and Fe (Renzini & Voli 1981). SNe Ia produce significantly more iron than oxygen or magnesium, as can be seen in Table 1. One can see that ^{56}Fe is clearly dominating the ejecta. It follows that SNe II must be the main contributor to the α-element enrichment.

Table 1. The most abundant elements ejected in a Type Ia supernova. In the calculations, Nomoto et al. (1984) assume accreting white dwarfs in close binary systems to be the progenitors of SN Ia events. The data refer to the W7 model; the values are given in $M_\odot$. The numbers show that the ejecta of SNe Ia are clearly dominated by ^{56}Fe.

^{12}C	3.2e-2	^{28}Si	1.6e-1	^{56}Fe	6.1e-1
^{16}O	1.4e-1	^{32}S	8.2e-2	^{57}Fe	1.1e-2
^{20}Ne	1.1e-2	^{36}Ar	2.2e-2	^{58}Ni	6.1e-2
^{24}Mg	2.3e-2	^{40}Ca	4.1e-2	^{60}Ni	1.1e-2

3.2 SNe II

As mentioned in the Introduction, we use two sets of models for the enrichment due to Type II supernova explosions: WW95 and TNH96.

The calculation of the SN II yields is affected by many uncertainties (see WW95, TNH96 and references therein). Elements lighter than iron like carbon, oxygen and magnesium are mainly produced during the evolutionary stages of the star *before* the explosion (Weaver & Woosley, in preparation). Thus, their abundances in the SN II ejecta are highly dependent on stellar evolution, especially on the $^{12}{\rm C}(\alpha,\gamma)^{16}{\rm O}$ rate during He-burning and the treatment of convection. Both a higher $^{12}{\rm C}(\alpha,\gamma)^{16}{\rm O}$ rate and the inclusion of semi-convection lead to a smaller production of carbon and carbon-burning products (TNH96).

The iron produced in hydrostatic silicon burning during the pre-supernova evolution forms the core of the star, which represents the minimum mass of the remnant. Depending on the position of the mass-cut and the fraction of mass falling back, the remnant mass can be higher (Nomoto & Hashimoto 1988; Hashimoto et al. 1993b; Weaver & Woosley 1993). The total amount of iron in the ejecta is exclusively produced during the explosion. More precisely, most of the explosively generated ^{56}Ni decays to ^{56}Fe. Thus, the theoretical iron yield of an SN II does not directly depend on parameters of stellar evolution, but on the simulation of the explosion itself.

Table 2 shows the important differences between the two sets. WW95 specify models A, B and C. In model B, the explosion energies are enhanced by a factor $\sim$1.5 in stars with $m \ge 30\,{\rm M}_\odot$, in model C by a factor $\sim$2 in stars with $m \ge 35\,{\rm M}_\odot$, both with respect to model A. TNH96 enhance the explosion energy for $m \ge 25\,{\rm M}_\odot$ by a factor of 1.5 with respect to the lower masses, as well. Hence, their models correspond best to model B in WW95. In the following, if not otherwise specified, the considered WW95 models are model B.

We discuss the differences in the yields of H, He, O, Mg, Fe and total ejected metals $Z_{\rm ej}$ as functions of the main-sequence mass of the star m ($M_\odot$). TNH96 evolve helium cores of mass m_α, adopting the relation between m and m_α from Sugimoto & Nomoto (1980). The total ejected mass of a certain element is then given by the calculated yield from the evolution of m_α plus the original element abundance in the envelope $m - m_\alpha$. Since TNH96 consider solar initial metallicity, for the discussion of the yields we assume the element abundances in the envelope to be solar. We use the solar element abundances from Anders & Grevesse (1989) – meteoritic values. It should be mentioned that the 70-$M_\odot$ star of the TNH96 results is not shown in the plots, but the relative yields are given in the captions.

3.2.1 *Ejected mass and hydrogen*

The left-hand panels in Fig. 1 show the total ejected masses. Models A (WW95) are characterized by the fall-back of envelope material in the high-mass range, an effect less pronounced in models B and

Table 2. The main differences in the SN II nucleosynthesis prescriptions of WW95 and TNH96. Models B and C in WW95 refer to enhanced explosion energies in high-mass stars by a factor of 1.5 and 2, respectively. TNH96 do not specify different models, but also enhance the explosion energy in high-mass stars by a factor of 1.5. Differences in stellar evolution [$^{12}C(\alpha,\gamma)^{16}O$ rate, convection theory] mainly affect the nucleosynthesis of intermediate elements lighter than iron. The yield of iron itself is highly dependent on the explosion.

	WW95	TNH96
$^{12}C(\alpha,\gamma)^{16}O$	1.7× Caughlan & Fowler (1988), 74 per cent of TNH96	Caughlan et al. (1985)
convection	Ledoux criterion, modification for semi-convection	Schwarzschild criterion, convective shells have greater extent
explosion energy	1.2×10^{51} erg (model A) model B: $E_B \approx 1.5\times E_A$ for $m \geq 30\,M_\odot$ model C: $E_C \approx 2\times E_A$ for $m \geq 35\,M_\odot$	1.0×10^{51} erg $E = 1.5\times10^{51}$ erg for $m \geq 25\,M_\odot$
explosion mechanism	piston situated at the Y_e discontinuity	deposition of energy
neutrinos	nucleosynthesis caused by the flood of neutrinos	neutrino process *not* included
mass grid	11, 12, 13, 15, 18, 19, 20, 22, 25, 30, 35, 40 $M_\odot$	13, 15, 18, 20, 25, 40, 70 $M_\odot$
initial metallicity	grid of 5 different Z_{in}	only solar Z_{in}
stellar evolution	entire stars	helium cores

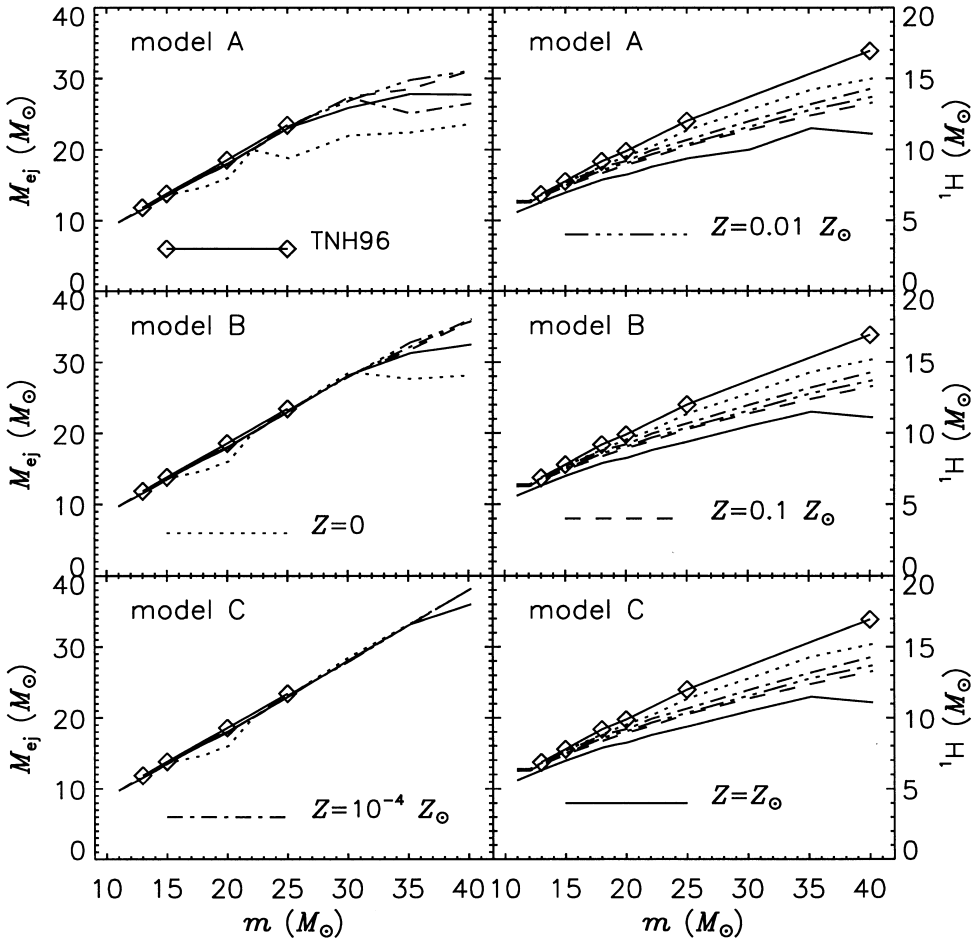

Figure 1. Total ejected mass (left-hand panels) and hydrogen yield (right-hand panels) of SNe II as a function of initial stellar mass ($M_\odot$). In each panel, one of the different linestyles is defined, indicating the five different initial metallicities assumed in WW95. The diamonds refer to the results of TNH96 ($Z_\odot$). The second and third rows show the results for enhanced explosion energy in high-mass stars in the calculations of WW95. The yields include initial and newly synthesized material. The hydrogen yield in the WW95 models shows a clear dependence on metallicity for high-mass stars.

Table 3. SN II ^{4}He yields according to WW95 ($Z_\odot$, model B) and TNH96. The numbers are given in $M_\odot$. Since Nomoto et al. (1997) do not give He yields, the considered (smaller) mass grid is taken from Thielemann et al. (1996).

	$13\,M_\odot$	$15\,M_\odot$	$20\,M_\odot$	$25\,M_\odot$
WW95	4.51	5.24	6.72	8.64
TNH96	4.13	4.86	5.95	6.63

virtually absent in models C. Except for the case $Z = 0$, the dependence on metallicity seems unimportant. The ejected masses in the WW95 and TNH96 models are very similar.

Conversely, the hydrogen yield (Fig. 1, right-hand panels) is clearly dependent on the initial metallicity of the star, especially at the high-mass end. Furthermore, for $m \gtrsim 20\,M_\odot$ the H yield given by TNH96 is larger than that in the WW95 models.

Both prescriptions basically agree in the value of $m_{\rm H} + m_{\rm He}$. Table 3 shows that the higher value for $m_{\rm H}$ corresponds to a lower helium yield in TNH96.

The difference in hydrogen (and then helium) yields comes from two causes: a different m_α–m relation at He ignition and the fact that TNH96 neglect the H-shell burning occurring after He ignition. In this respect we notice that in the WW95 models, the m_α of a 25-$M_\odot$ star is 9.21 $M_\odot$, 1.21 $M_\odot$ larger than that adopted by TNH96 for the same initial mass, on the basis of the m_α–m relation by Sugimoto & Nomoto (1980). The He yield of this star is 2 $M_\odot$ larger than in the TNH96 models, reflecting the He production due to the H-burning shell. A fair comparison between the predictions of the two sets of models should be done at constant m_α. However, since we lack the m_α-values for WW95 models for masses other than $25\,M_\odot$, we proceed by comparing the element production for the same initial mass.

3.2.2 *Oxygen and metallicity*

The yield of oxygen and total ejected mass of all elements heavier than helium (Z) are plotted in Fig. 2. The figure shows that Z is clearly dominated by oxygen. Both depend only weakly on initial metallicity except for the $Z_{\rm in} = 0$ case. The results of WW95 and TNH96 are similar, except that TNH96 produce more oxygen in the higher mass range. This can be understood in terms of the higher $^{12}C(\alpha,\gamma)^{16}O$ rate in the TNH96 models. It is worth noting that the large difference in the yields of high-mass stars may also result from the fact that WW95 consider fallback of material, whereas TNH96

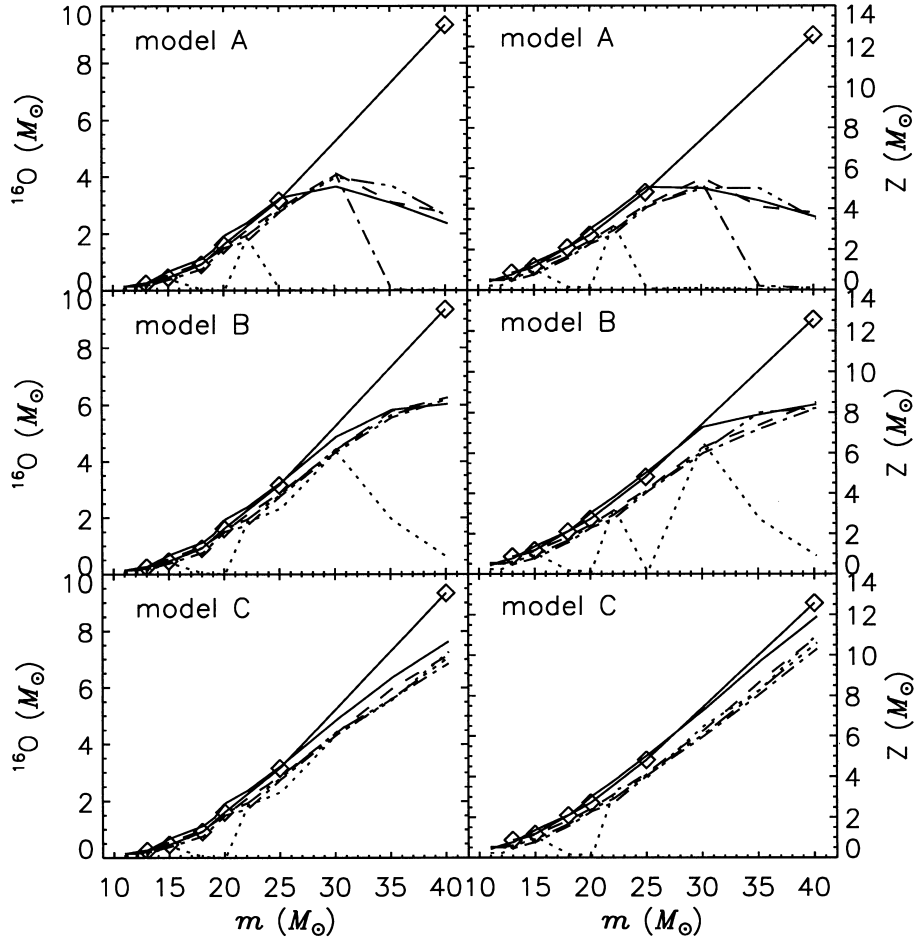

Figure 2. Oxygen yield (left-hand panels) and ejected metallicity (right-hand panels) of SNe II as a function of initial stellar mass ($M_\odot$). The different linestyles and symbols are explained in Fig. 1. The yields include initial and newly synthesized material. The figure demonstrates that oxygen is clearly dominating the total metallicity of the ejecta. The dependence on initial metallicity of the star seems negligible (except for $Z_{\rm in} = 0$). The oxygen yield of the 70-$M_\odot$ star according to TNH96 is $\sim$22 $M_\odot$.

Table 4. SN II yields of the elements C and O and the main carbon-burning products; comparison of WW95 ($Z_\odot$, model B) and TNH96. The numbers are given in units of $M_\odot$. The TNH96 numbers consist of the given yield from helium core evolution plus the initial abundance (solar) of the envelope (see text). In spite of the systematically larger ^{12}C yield, WW95 give less ^{24}Mg in most of the stars, although magnesium is a carbon-burning product. Due to WW95, this pattern is caused by the different convection theories (see text).

		13 $M_\odot$	15 $M_\odot$	18 $M_\odot$	20 $M_\odot$	25 $M_\odot$	40 $M_\odot$
^{12}C	WW95	1.14(−1)	1.61(−1)	2.48(−1)	2.13(−1)	3.22(−1)	3.63(−1)
	TNH96	3.21(−2)	1.16(−1)	2.04(−1)	1.56(−1)	2.00(−1)	2.21(−1)
^{16}O	WW95	2.72(−1)	6.80(−1)	1.13	1.94	3.25	6.03
	TNH96	2.44(−1)	4.60(−1)	9.17(−1)	1.61	3.15	9.34
^{20}Ne	WW95	4.46(−2)	1.11(−1)	2.77(−1)	1.05(−1)	3.94(−1)	1.24
	TNH96	3.82(−2)	3.86(−2)	1.82(−1)	2.52(−1)	6.22(−1)	6.97(−1)
^{23}Na	WW95	1.08(−3)	3.42(−3)	9.99(−3)	1.53(−3)	1.08(−2)	3.68(−2)
	TNH96	1.05(−3)	5.20(−4)	7.68(−3)	1.62(−3)	1.87(−2)	2.45(−2)
^{24}Mg	WW95	1.64(−2)	2.67(−2)	5.52(−2)	3.13(−2)	1.06(−1)	2.30(−1)
	TNH96	1.42(−2)	3.73(−2)	4.29(−2)	1.54(−1)	1.68(−1)	3.66(−1)

do not. The O yield of TNH96 increases rapidly with mass; the WW95 yields, instead, seem to saturate. This discrepancy already indicates that there is a huge uncertainty concerning the stellar yields of high-mass stars ($m > 40\,M_\odot$).

At the lower mass range ($m \leq 20\,M_\odot$), WW95 yields tend to be slightly larger for the same metallicity ($Z_\odot$), possibly because of the larger m_α. However, the similarity of the results of the two sets of models suggests that the uncertainty in the oxygen yield from SNe II is small.

3.2.3 Magnesium and iron

Both WW95 and TNH96 produce an Mg yield with a rapid rise in a certain mass range at $M \approx 18\,M_\odot$ for TNH96 and at $M \approx 23\,M_\odot$ for WW95. As a consequence, in the mass range $18 - 25\,M_\odot$, the Mg yield of TNH96 is larger by about a factor of $3 - 5$. We will briefly investigate the origin of this discrepancy, which, as we will show, is very significant in the context of chemical evolution.

^{24}Mg is mainly produced during hydrostatic carbon burning. Thus, Table 4 gives the yields of ^{12}C, ^{16}O and the main carbon-burning products ^{20}Ne, ^{23}Na and ^{24}Mg (Arnett & Thielemann 1985). ^{24}Mg is produced in the following reaction (Arnett & Thielemann 1985):

$$^{12}\mathrm{C}(\,^{12}\mathrm{C},\mathrm{p})\,^{23}\mathrm{Na}(\mathrm{p},\gamma)\,^{24}\mathrm{Mg}.$$

Hence, the model producing more carbon should also produce more magnesium. Table 4 shows that the carbon yields are systematically higher in WW95 for all stellar masses. This is reasonable when taking into account the larger helium cores[2] and the lower $^{12}\mathrm{C}(\alpha,\gamma)^{16}\mathrm{O}$ rate of WW95. However, for the yields of ^{20}Ne, ^{23}Na and ^{24}Mg this is not the case for all masses. In general, for low-mass stars ($m \leq 18\,M_\odot$) the yields of the carbon-burning products ^{20}Ne and ^{23}Na are higher in WW95 models as well. With the exception of the 40-$M_\odot$ star, the higher masses exactly invert this pattern. The yield of ^{24}Mg behaves similarly, but the effect is much stronger with the largest discrepancy for the 20-$M_\odot$ star. WW95 argue that the larger extent of the convective shells in the TNH96 models (Schwarzschild criterion) is responsible for the above behaviour. Since the observations of magnesium overabundance can be better explained with high Mg yields in SNe II (see following sections), this could be interpreted as an argument in favour of the Schwarzschild criterion in convection theory.

[2]Carbon is a helium-burning product.

Similarly to the O yields, the Mg yields of WW95 seem to saturate or even decline for increasing mass above 40 $M_\odot$, due to re-implosion. According to the TNH96 calculations, instead, a huge amount of magnesium is ejected by high-mass stars.

Fig. 3 shows that the iron yield declines for masses between 13 and 20 $M_\odot$ in both sets of models. The iron yields in the lower mass range are very similar; both models match the observational constraints at 14 $M_\odot$ (SN1993J: e.g. Baron, Hauschildt & Young 1995; Nomoto, Iwamoto & Suzuki 1995) and 20 $M_\odot$ (SN1987A: e.g Arnett et al. 1989). Table 5 shows that both groups can reproduce the observed ^{56}Ni of the supernova events, which is dominating the iron yield. Thus, in the lower mass range, TNH96 and WW95 basically agree on the Fe yield.

However, WW95 produce significantly more iron than TNH96 in stars of $m \geq 25\,M_\odot$, especially in models B and C. Thus, mainly this mass range will be responsible for discrepancies in the Fe yields of the total mass range of SNe II (for SSP yields, see Section 4).

3.3 IMF-weighted yields

For the discussion of chemical evolution, it is more meaningful to consider stellar yields weighted by the IMF. Normalized on the SN II yield of the whole mass range, these values give the relative contribution of a 1-$M_\odot$ interval to the total SN II yield. To show the role of various mass intervals in the enrichment of a certain element, we plot the IMF-weighted yields of the elements oxygen, magnesium and iron, and metallicity for different IMF slopes and both nucleosynthesis models WW95 and TNH96. In more detail, we plot the following quantity:

$$\frac{\mathrm{d}Q_{im}}{\mathrm{d}m} = \frac{Q_{im} \times \phi(m)}{\int_{11}^{40} Q_{im} \times \phi(m)\mathrm{d}m}. \qquad (17)$$

The figures are given in Appendix A. Summarizing the plots, we obtain the following results:

(i) there is no specific mass range dominating the O and Z enrichment significantly for all considered IMF slopes;

(ii) the IMF-weighted Mg yield is slightly peaked at 30 $M_\odot$ (WW95) and 20 $M_\odot$ (TNH96), but again these masses do not dominate the SSP yield significantly;

(iii) the Fe enrichment due to SNe II, instead, is clearly governed by stars of $m \leq 20\,M_\odot$.

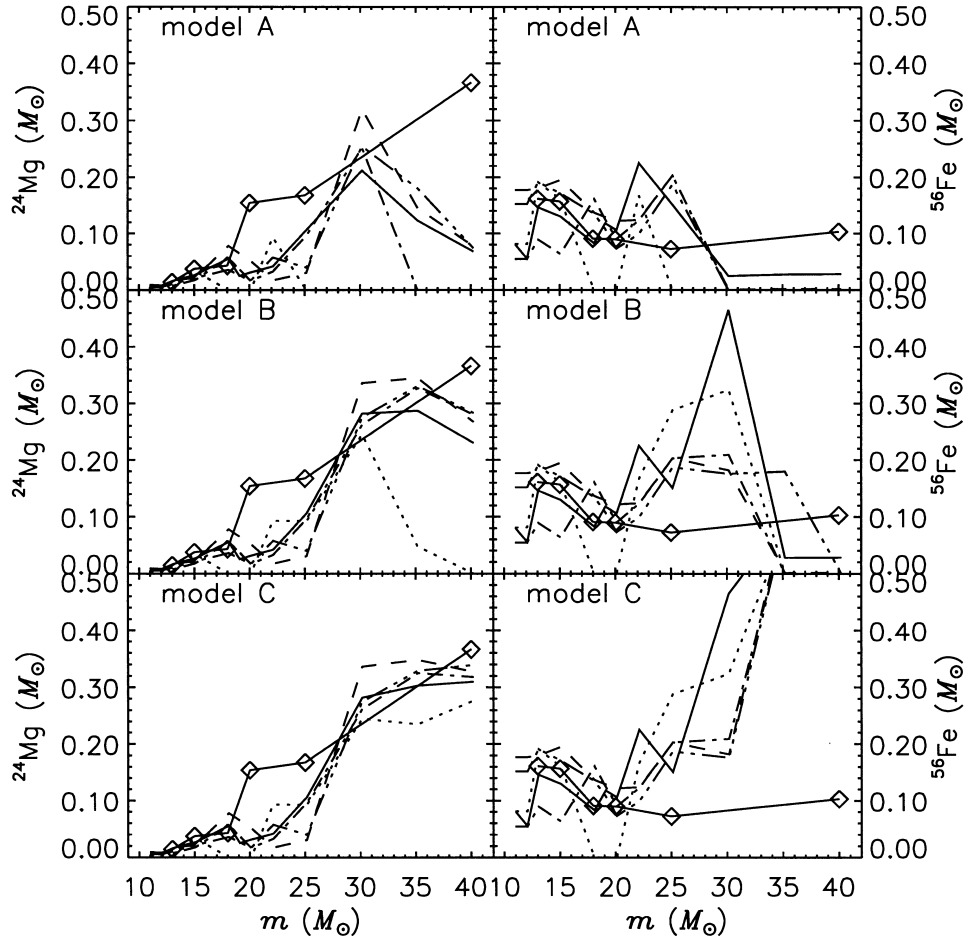

Figure 3. Magnesium yield (left-hand panels) and iron yield (right-hand panels) of SNe II as a function of initial stellar mass ($M_\odot$). The different linestyles and symbols are explained in Fig. 1. The yields include initial and newly synthesized material. The dependence of both the Mg and Fe yields on initial metallicity is not very clear. TNH96 and WW95 agree very well in the Mg and Fe yields for low-mass stars. The magnesium and iron yields of the 70-$M_\odot$ star according to TNH96 are ~0.8 and ~0.1 $M_\odot$, respectively.

Table 5. Theoretical and observed ejected ^{56}Ni ($M_\odot$) in the SN II events SN1993J (14 $M_\odot$: Arnett et al. 1989) and SN1987A (20 $M_\odot$: Baron et al. 1995; Nomoto et al. 1995). The observational data are compared with the theoretical results of TNH96 and WW95. Both nucleosynthesis prescriptions are in agreement with observation.

m_* ($M_\odot$)	observation	WW95 ($Z_\odot$)	TNH96
14 ± 1	0.100 ± 0.02	$0.133 - 0.115$	$0.153 - 0.130$
20	0.075 ± 0.01	0.088	0.074

Altogether, the plots demonstrate the increasing weight of the higher mass range with decreasing IMF slope x.

3.4 The ratio [Mg/Fe]

In Fig. 4, we plot the abundance ratio [Mg/Fe] produced in WW95 ($Z_\odot$) and TNH96 as a function of stellar mass. The figure shows that the ratio of magnesium to iron is basically increasing with mass. In the intermediate-mass range, the overabundance in TNH96 models exceeds the results of WW95 significantly. The maximum overabundance in TNH96 is reached in the most massive star ($m = 70\,M_\odot$), whereas the Mg/Fe of the WW95 models peaks at $m = 35\,M_\odot$.

According to WW95, a magnesium overabundance is only produced in stars with $m \gtrsim 25\,M_\odot$ (except for the small peak at $m = 18\,M_\odot$). Thus, in the first ~10 Myr, when the turn-off is above $20\,M_\odot$ (see upper x-axis in Fig. 4), these stars will enrich the ISM with highly magnesium-overabundant ejecta. However, already 30 Myr after the beginning of star formation, the turn-off of $10\,M_\odot$ is reached and the whole SN II generation of stars is contributing to the enrichment. Thus, the key value for the discussion of chemical evolution is the SSP yield.

4 SSP YIELDS

We calculated SSP yields of the elements oxygen, magnesium and iron in the mass range of SNe II for different IMF slopes and both sets of SN II nucleosynthesis. The tables in Appendix B give the abundances of the considered elements in the ejecta of SN II explosions of one SSP ($m_{\rm max} = 40\,M_\odot$). The basic conclusions for the discussion of the yields are as follows.

(i) The highest [Mg/Fe] ratio in WW95 is produced in model B assuming an initial metallicity of $Z = 10^{-4}\,Z_\odot$. This ratio is lowest for models C because of the high iron yield.

(ii) The second highest value for [Mg/Fe] is produced in the models with $Z = Z_\odot$. The results for $Z = 0.01\,Z_\odot$ and $0.1\,Z_\odot$ are in

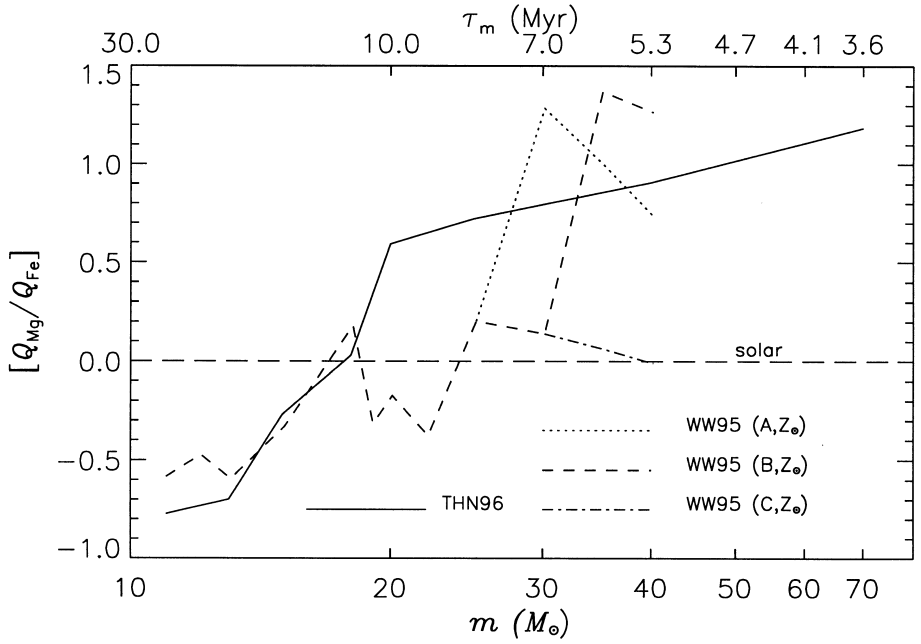

Figure 4. Abundance ratio of magnesium to iron in the ejecta of SNe II as a function of initial stellar mass. The values are normalized on solar values and plotted on a logarithmic scale. The WW95 models of solar initial metallicity are considered. The upper x-axis denotes the lifetime τ_m of the star with mass m (Schaller et al. 1992). Mainly stars in the upper mass range contribute to super-solar [Mg/Fe] ratios.

between. Hence, [Mg/Fe] is neither increasing nor decreasing with initial metallicity. The high and low WW95 metallicities *do not* bracket the expected SSP yields as claimed by Gibson, Loewenstein & Mushotzky (1997).

(iii) TNH96 produce systematically higher [Mg/Fe] ratios than WW95.

For the Salpeter IMF, the magnesium abundance in the SN II ejecta is 0.13 dex higher with TNH96 models than with WW95 models. The iron abundance, instead, is 0.08 dex lower. In total, this leads to a [Mg/Fe] ratio which is 0.21 dex higher for TNH96 nucleosynthesis.

We define the *time-dependent* SSP yield for element i at time t as

$$Q^i_{\rm SSP}(t) = \frac{\int_{m_{\rm t}}^{m_{\rm max}} Q_{im}\,\phi(m){\rm d}m}{\int_{m_{\rm t}}^{m_{\rm max}} (1-w_m)\,\phi(m){\rm d}m}. \qquad (18)$$

This equation describes the abundance of element i in the ejecta of one generation of stars of one single metallicity at the time t. With progression of time, the turn-off mass decreases and $Q^i_{\rm SSP}(t)$ converges to the standard SSP yield, integrated over the whole mass range. We consider enrichment due to PNe, SNe II and SNe Ia (see also equation 8). Since TNH96 models are computed only for solar metallicities, we consider WW95 yields of solar initial metallicity. The stellar lifetimes are taken from Schaller et al. (1992). For the following computations we have extrapolated TNH96 yields to $11\,{\rm M}_\odot$, and neglected the contribution from SNe II coming from stars with masses in the range $8-11\,{\rm M}_\odot$ (see WW95). The fraction of close binary systems is $A = 0.035$. As discussed in Section 5, this value is calibrated in the chemical evolution model of the solar neighbourhood. Since the value of this parameter is very small, the yields of SNe II are only marginally affected by the choice of A. The exact number becomes important when star formation time-scales of $\sim$10 Gyr and enrichment due to SNe Ia are considered. For the remnant masses, we adopt Renzini & Voli (1981) up to $8\,{\rm M}_\odot$, and either WW95 or TNH96 from 11 to $40\,{\rm M}_\odot$. In the range $8-11\,{\rm M}_\odot$ the mass of the remnant is taken to be $1.4\,{\rm M}_\odot$.

4.1 Magnesium

Fig. 5 shows the abundance of magnesium in the ejecta of one dying generation of stars as a function of turn-off mass. The abundances are normalized to solar values and plotted on a logarithmic scale. The magnesium abundance in the ejecta is significantly super-solar. The upper x-axis shows the progression of time which is not linear with the turn-off mass. The turn-off of $3\,{\rm M}_\odot$ is reached after 0.341 Gyr, but it takes more than 7 Gyr until stars of $1\,{\rm M}_\odot$ contribute to the enrichment as well. The different line styles belong to various IMF slopes. The solid line indicates the Salpeter IMF.

One can see that the magnesium abundance in the total ejecta is decreasing with turn-off mass for $m_{\rm t} < 20\,{\rm M}_\odot$. This is due to the fact that most magnesium is processed in stars more massive than $20\,{\rm M}_\odot$ (Fig. 3). The SN II SSP yield is reached at $m_{\rm t} = 8\,{\rm M}_\odot$. For $m_{\rm t} \leq 8\,{\rm M}_\odot$, SNe Ia and PNe begin to contribute. However, since both events do not eject a significant amount of magnesium (see Table 1), the abundance is still decreasing with decreasing turn-off mass and increasing time.

The most striking aspect of this diagram is that the magnesium abundance due to TNH96 nucleosynthesis is 0.13 dex higher than the value provided by WW95 (Salpeter IMF, model B). This is caused by the significant difference in the yields of $18-25\,{\rm M}_\odot$ stars as shown in Fig. 3. Hence, the discrepancy between WW95 and TNH96 is maximum at $m_{\rm t} \approx 19\,{\rm M}_\odot$.

4.2 Iron

The iron enrichment of the SSP as a function of time is shown in Fig. 6. Since iron is mainly synthesized in stars of lower masses, the

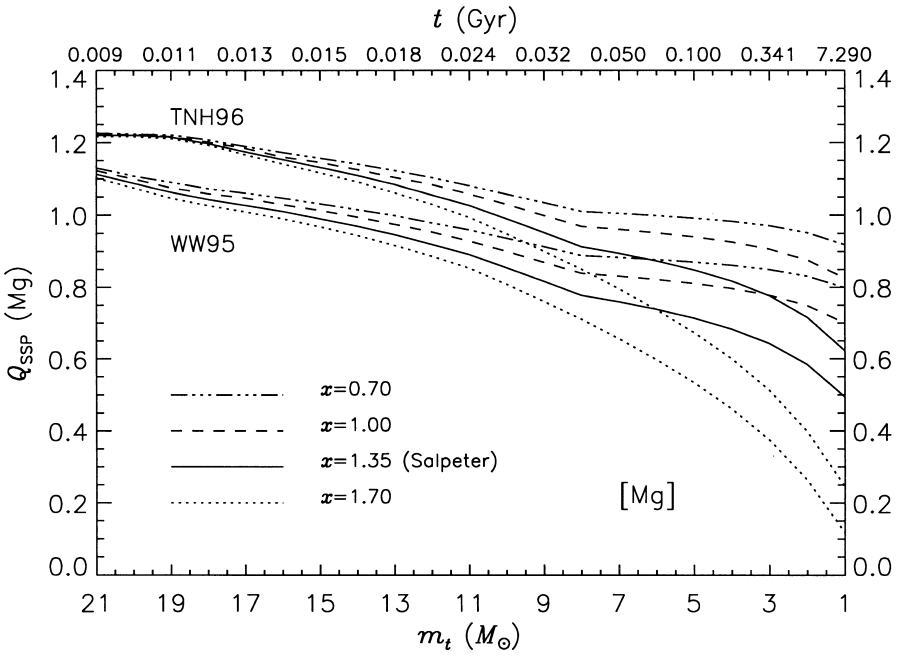

Figure 5. The figure shows the abundance of magnesium in the ejecta of one generation of stars in the range from the turn-off to the maximal mass $m = 40\,\mathrm{M}_\odot$. This mass range is increasing with decreasing turn-off mass m_t (lower x-axis) and with increasing time (upper x-axis). The quantity Q_SSP is defined in equation (18). The enrichment due SNe II ($11 - 40\,\mathrm{M}_\odot$), SNe II ($3 - 16\,\mathrm{M}_\odot$) and PNe ($1 - 8\,\mathrm{M}_\odot$) is taken into account. The fraction $A = 0.035$ of binaries exploding as SNe Ia is determined in the chemical evolution model for the solar neighbourhood in Section 5. The calculated SSP yield (see equation 18) is normalized on the solar magnesium abundance (Anders & Grevesse 1989) and plotted on a logarithmic scale. Different SSP yields are calculated for different IMF slopes x and SN II yields [TNH96, WW95(B, $\mathrm{Z}_\odot$)]. The total contribution of SNe II to the SSP yield is reached after 24 Myr when the turn-off mass is $11\,\mathrm{M}_\odot$. Since mainly high-mass stars contribute to the enrichment of magnesium, the SSP yield is decreasing with decreasing turn-off mass. For the Salpeter IMF, the abundance of magnesium in the ejecta of SNe II is 0.13 dex higher using TNH96 yields.

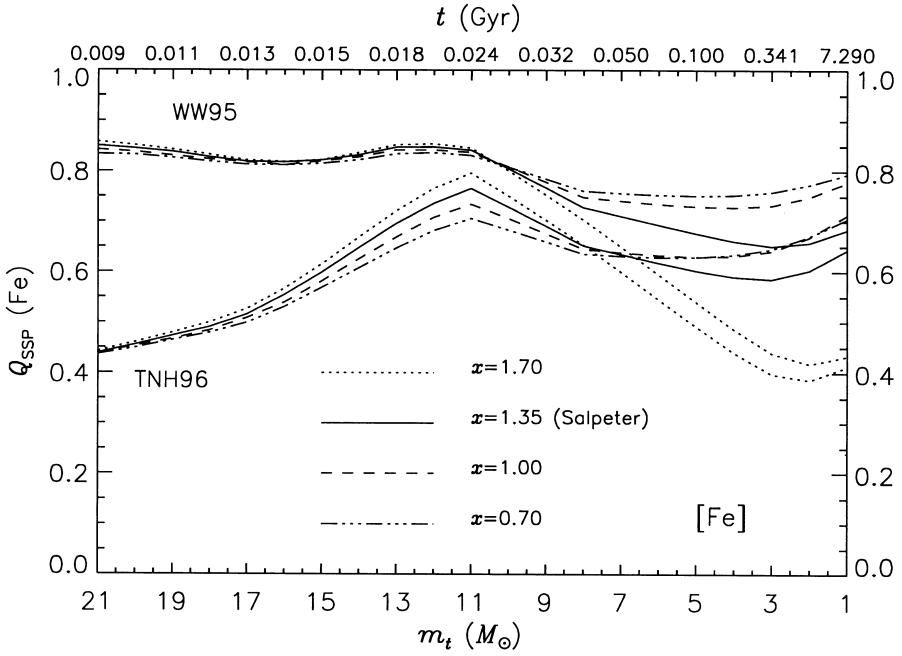

Figure 6. The figure shows the abundance of iron in the ejecta of one generation of stars in the range from the turn-off to the maximal mass $m = 40\,\mathrm{M}_\odot$. For a detailed description see the caption of Fig. 5. Since low-mass stars dominate the iron yield of SNe II, the maximal SN II SSP yield is reached at $m_\mathrm{t} = 11\,\mathrm{M}_\odot$. The value decreases with the contribution of PNe and rises again when SNe Ia enter the game. For the Salpeter IMF, the SN II yields of WW95 lead to an iron abundance which is 0.08 dex higher.

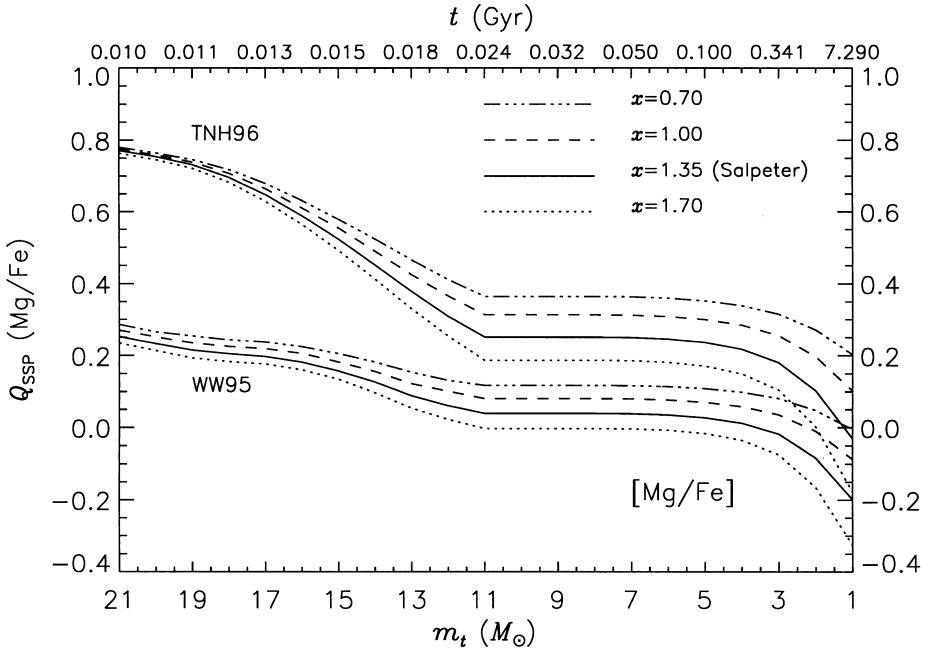

Figure 7. The figure shows the abundance ratio of magnesium over iron in the ejecta of one generation of stars in the range from the turn-off to the maximal mass $m = 40\,M_\odot$. For a detailed description see the caption of Fig. 5. Since stars between 8 and 11 $M_\odot$ do neither eject magnesium nor iron, the ratio is constant in this mass range. The further ejection of iron due to SNe Ia drives the ratio down for lower turn-off masses. The ratio provided by the SNe II yields of WW95 does not suffice to explain magnesium-enhanced abundance ratios, even for $x = 0.70$.

time-dependent SSP yield is roughly constant (WW95) or even increasing (TNH96) with increasing turn-off mass (Fig. 6) until the SN II value is reached. Since stars between 8 and 11 $M_\odot$ are assumed not to contribute to the enrichment of heavy elements, there is a peak at 11 $M_\odot$. At late times, the contribution due to SNe Ia comes into play, and the iron abundance in the ejecta is rising again. It is important to recognize that the iron abundance in the ejecta of SNe II is higher for a steeper IMF (see dotted curve). The results from TNH96 models are more strongly dependent on the slope of the IMF than WW95 results, because the contribution of high-mass stars to the iron production is smaller in TNH96 (see also figure 4). For the same reason, the difference between WW95 and TNH96 increases for a flatter IMF.

4.3 [Mg/Fe]

Fig. 7 shows the following aspects.

(i) In the first 10 Myr, the produced magnesium overabundance is fairly high; the difference between WW95 and TNH96 is extremely large. WW95 yields reach [Mg/Fe] ≈0.2 at a turn-off $m_t \approx 20\,M_\odot$, after 10 Myr. Even considering a flat IMF with $x = 0.70$, the minimum overabundance in ellipticals of 0.2 dex (Worthey et al. 1992) is reached at $t \approx 15$ Myr when the contribution of SNe II is not yet complete. TNH96 provide the same value of [Mg/Fe] after 7.3 Gyr when SN Ia explosions have already reduced the ratio. Obviously, this strongly affects the time-scales of star formation of a system showing an [Mg/Fe] overabundance.

(ii) One generation of SN II exploding stars cannot produce the magnesium overabundance in metal-poor stars in the solar neighbourhood, when considering the Salpeter IMF and WW95 SN II yields. Assuming a value of [Mg/Fe] ≈0.3 – which is already a lower limit – all low-metallicity stars should have been born in the first 9 million yr (see also Section 5).

(iii) With the progression of time, the overabundance is decreasing, because more and more low-mass stars ($m < 20\,M_\odot$) with higher iron and lower magnesium yields are contributing to the enrichment. Once the turn-off mass is 8 $M_\odot$, the final SN II SSP value is reached.

(iv) The magnesium overabundance in the SN II output increases according to the flattening of the IMF. This is a result of giving more weight to magnesium-producing high-mass stars.

(v) The dependence of [Mg/Fe] on the IMF slope is increasing with time. This is understandable, because for a larger considered mass range the role of the IMF slope becomes more important.

(vi) The TNH96 models provide an [Mg/Fe] ratio of 0.26 dex, WW95 models lead to [Mg/Fe] = 0.05 dex, both for the Salpeter IMF.

WW95 specify an uncertainty of a factor of 2 in the iron yield. Since this causes a shift by 0.3 dex, one could argue that simply taking half of the iron yield would solve the overabundance problem. We want to show that this is not the case. Since the iron yields of stars below 20 $M_\odot$ are very similar in the two sets of models, and since both sets reproduce the observations of SN1987A and SN1993J very well (see table 5), it is reasonable only to halve the iron yields of stars above 20 $M_\odot$ in WW95. Re-calculating the SSP yields with the modified Fe yield of WW95, it turns out that the total [Fe] is only shifted by 0.08 dex to lower values. Fig. 8 shows the [Mg/Fe] ratio as a function of the turn-off mass in this experiment. The plot shows that it remains difficult to reproduce the observed magnesium overabundances with WW95 nucleosynthesis.

It is important to mention also that TNH96 magnesium yields may not suffice to explain observed [Mg/Fe] overabundances in elliptical galaxies. There are several indications that [Mg/Fe] in the nuclei of ellipticals does even exceed 0.4 dex (Weiss et al. 1995; Mehlert et al. 1998). As demonstrated in Fig. 7, this value cannot be

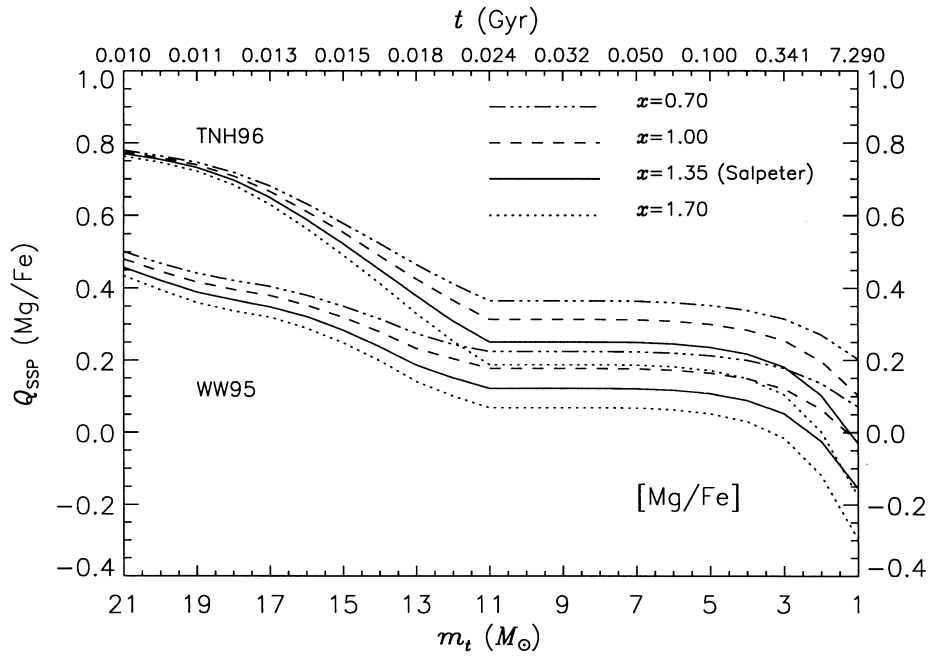

Figure 8. The diagram shows the same as Fig. 7. In addition, we have assumed a reduced WW95 iron yield for masses above 20 $M_\odot$ by a factor of 2, according to the uncertainty given in WW95. The iron yields of masses below 20 $M_\odot$ are not overestimated by a factor of 2 in WW95, because they agree with the observations of SN1987A and SN1991J (see text). The SN II SSP yield of iron is increased by 0.08 dex, which is not enough to improve the situation significantly.

theoretically produced by one SN II-exploding generation of stars. Hence, claiming [Mg/Fe] $\gtrsim$0.4 dex, the star-forming phase in giant ellipticals must be of the order of 10^7 yr, even for TNH96 yields and a flat IMF ($x = 0.7$). A detailed exploration of star formation timescales, IMF slopes and stellar yields in elliptical galaxies will be the subject of a forthcoming paper.

Finally, one should not forget that the number of input parameters in the calculations is very small. The above conclusions do not depend on galaxy formation scenarios, on star formation histories, on infall models, or on binary fractions. The only considered parameters are the IMF slope and stellar yields.

4.4 [O/Fe]

Fig. 9 shows the time-dependent SSP yield as a function of turn-off mass for the abundance ratio [O/Fe]. Since both oxygen and magnesium are produced mainly in SNe II, one would expect similar values for the overabundance.

For TNH96, this is exactly the case. The contribution of low-mass stars ($1 \leq m \leq 8\,M_\odot$) to the enrichment of oxygen manifests itself in an elongation of the SN II plateau down to 5.5 $M_\odot$. Although SNe Ia produce 6 times more oxygen than magnesium, the SNe Ia reduce [O/Fe] by approximately the same amount because of the dominant role of iron in the ejecta. The WW95 [O/Fe] ratio, instead, is 0.12 dex higher than [Mg/Fe].

The discrepancy between WW95 and TNH96 [O/Fe] ratios now originates mainly from the discrepancy in the iron yields, while oxygen yields differ by 0.02 dex. This leads again to the conclusion that WW95 may underestimate the magnesium yield.

4.5 On the upper mass cut-off

In this section, we will investigate the influence of a variation of the upper mass cut-off on the calculated SSP yields. For this purpose, we include the results of TNH96 for the 70-$M_\odot$ star. In order to compare the different nucleosynthesis prescriptions, we have to extrapolate the WW95 yields to higher masses, hence the result has to be interpreted with caution. In the WW95 models most heavy elements re-implode for the massive stars, so that the contribution of these stars to the enrichment is negligible. Indeed, the plots in Figs 2 and 3 show this trend for the elements oxygen and magnesium, respectively (also model B). TNH96 do not consider fallback, thus their O–Mg yields increase with mass up to $m = 70\,M_\odot$.

Table 6 gives the variation of the abundances of various elements in the SN II ejecta of one SSP, if $m_{\rm max} = 70\,M_\odot$ with respect to the $m_{\rm max} = 40\,M_\odot$ case. These reflect both the metal production and the total ejected mass in the range $40 - 70\,M_\odot$. The following striking aspects should be noted.

(i) The iron abundance in the ejecta decreases for all models. This effect is strongest for flatter IMF and WW95 models.

(ii) The oxygen abundance, instead, increases for all models. Again the effect is strongest for a flatter IMF, but more important in TNH96.

(iii) The behaviour of the magnesium abundance is more complex. For TNH96 the increase of magnesium becomes more significant with a flatter IMF, whereas for WW95 the pattern is the reverse.

In total, the [Mg/Fe] ratio in the SSP ejecta increases significantly only for the TNH96 models. In the WW95 models, the effect of fallback prevents a significant change. This is confirmed in Fig. 10 in which we show the abundance ratios as a function of turn-off mass and time with $m_{\rm max} = 70\,M_\odot$ considered. The diagram shows that by assuming a larger value for $m_{\rm max}$ the problem of the magnesium overabundance is relaxed, *if the high Mg yield calculated by TNH96 in high-mass stars is correct.* This seems to us still controversial. It is of great importance in the future to improve our knowledge on the stellar yields of these stars, too.

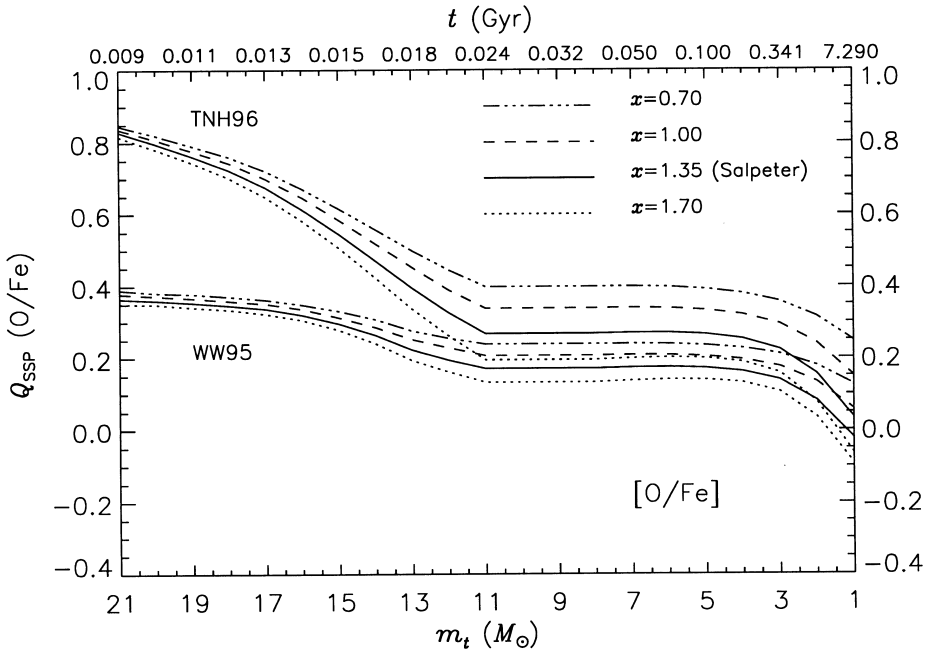

Figure 9. The figure shows the abundance ratio of oxygen over iron in the ejecta of one generation of stars in the range from the turn-off to the maximal mass $m = 40\,M_\odot$. For a detailed description see the caption of Fig. 5. Oxygen and magnesium overabundances in the ejecta of SNe II are the same in the case of TNH96 yields. With WW95, instead, the SSP value of [O/Fe] is ∼0.12 dex higher than [Mg/Fe]. Since both are α-elements and should therefore be enhanced by approximately the same amount, this is a further indication that WW95 underestimate the magnesium yield of SNe II.

Table 6. The numbers give the shift of the abundances in the ejecta of one SSP when the maximum mass is increased from 40 to 70 $M_\odot$. The yields of WW95 are extrapolated to masses above 40 $M_\odot$.

	$x = 1.7$			$x = 1.35$			$x = 1.0$			$x = 0.7$		
	Δ[O]	Δ[Mg]	Δ[Fe]	Δ[O]	Δ[Mg]	Δ[Fe]	Δ[O]	Δ[Mg]	Δ[Fe]	Δ[O]	Δ[Mg]	Δ[Fe]
TNH96	0.20	0.14	−0.01	0.23	0.17	−0.01	0.26	0.19	−0.01	0.28	0.22	−0.02
WW95	0.09	0.02	−0.03	0.11	0.02	−0.05	0.12	0.01	−0.06	0.13	0.00	−0.09

Furthermore, it is worth noting that the abundance ratio of magnesium to oxygen decreases with the inclusion of stars more massive than 40 $M_\odot$. This is important because it becomes even more difficult to reproduce the solar Mg/O ratio. We give a detailed exploration of this aspect in Section 5.3.

5 THE SOLAR NEIGHBOURHOOD

5.1 The model parameters

The chemical evolution of our Galaxy has been treated in the literature several times (e.g. Matteucci & Greggio 1986; Timmes et al. 1995; Pagel & Tautvaisiene 1995; Tsujimoto et al. 1995, Yoshii, Tsujimoto & Nomoto 1996). The model predictions fit the data quite well: the main observational features can be reproduced. In the classical numerical models, the chemical evolution of the ISM in the solar neighbourhood is described in a one-zone model of homogeneous and instantaneously mixing gas. The latter assumption is called the instantaneous mixing approximation. The instantaneous recycling approximation, which neglects the stellar lifetimes, is relaxed in these models as well as in our calculations. In principle, the accretion of gaseous matter over a time-scale of ∼4 Gyr enables us to avoid the formation of extremely metal-poor stars with [Fe/H]< −3, known as the G-dwarf problem (Larson 1972; Tosi 1988; Matteucci & François 1989). The formation of the disc in the solar vicinity due to accretion $f(t)$ is described in the following equation (Timmes et al. 1995):

$$f(t) = [M_{\rm tot}(t_{\rm now}) - M_{\rm tot}(t_0)] \times \frac{\exp(-t/\tau_{\rm disc})}{\tau_{\rm disc}[1 - \exp(-t_{\rm now}/\tau_{\rm disc})]}\ , \qquad (19)$$

with $M_{\rm tot}(t_{\rm now} = 15$ Gyr) and $M_{\rm tot}(t_0 = 0$ Gyr) as the surface densities ($M_\odot\,{\rm pc}^{-2}$) of the total mass (stars+gas) today and at the beginning of the disc formation, respectively. The accretion time-scale for the formation of the disc is controlled by the parameter $\tau_{\rm disc}$.

The SFR is assumed to depend on the gas density of the ISM (Schmidt 1959, 1963) with ν (Gyr^{-1}) as the efficiency of star formation (free parameter):

$$\psi(t) = \nu M_{\rm tot}\left[\frac{M_{\rm g}(t)}{M_{\rm tot}(t)}\right]^k . \qquad (20)$$

In the literature, the adopted value for the exponent k varies between $k = 1$ and 2 (e.g. Matteucci & François 1989). In the following section, we will show the influence of this parameter on the observational features. The Schmidt law, together with the infall of gas over a relatively long time-scale, guarantees roughly

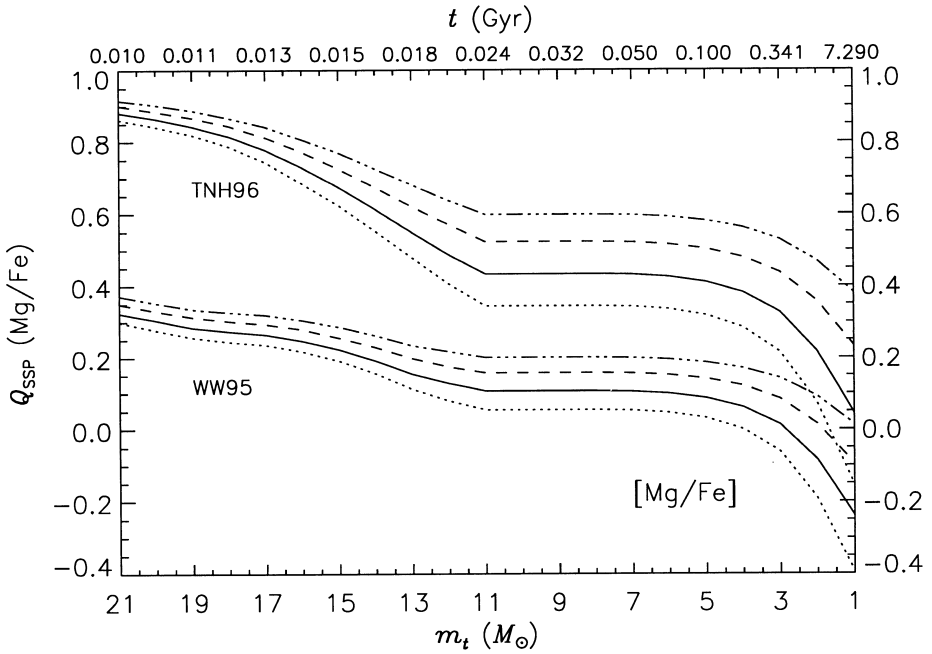

Figure 10. The figure shows the abundance ratios of magnesium over iron in the ejecta of one generation of stars in the range from the turn-off to the maximal mass $m = 70\,M_\odot$. For a detailed description see the caption of Fig. 5. The consideration of a higher maximum mass leads to larger [Mg/Fe] ratios for TNH96 models. The results for WW95 basically do not change. However, the WW95 yields are extrapolated to $70\,M_\odot$ and are therefore uncertain.

Table 7. Input parameters in the calculations for the chemical evolution of the solar neighbourhood. The parameters are chosen to match simultaneously the observational constraints: ADF, AMR, supernova rates, solar element abundances, current infall rate, and current fraction of gaseous mass. The second column shows the main observational constraints on the respective parameter. The third column gives the final adopted values.

Parameter	Observational constraint	Adopted value
Stellar yields	Element abundances of the Sun	TNH96
IMF slope x	Solar abundance ratios	1.36
Close binary fraction A	Relative frequency of Type II and Ia SNe AMR	0.035
Star formation efficiency ν	current fraction of gaseous mass	1.3 Gyr^{-1}
Schmidt exponent k	ADF	2
Accretion time-scale τ_{disc}	current infall rate ADF	4 Gyr

continuous star formation during the evolution of the solar neighbourhood.

Furthermore, the enrichment of the ISM due to PNe, SNe II and SNe Ia is considered, using supernova rates as described in Section 2. The parameter A in equations (10) and (11) is a free parameter. It is calibrated on the current supernova rates in our Galaxy. As shown in the previous sections, in particular the yields of SNe II are affected by many uncertainties. Hence, we treat the SN II yields as a parameter in the sense that we consider the different SN II nucleosynthesis prescriptions presented in Section 3 (WW95 and TNH96). TNH96 yields consist of the given yield from the evolution of the helium core plus the initial abundance of the element in the envelope (see also Section 3). In the simulations of the chemical evolution, the initial element abundances of the envelopes correspond to the element abundances in the ISM when the star forms. In these terms, the TNH96 yields become metallicity-dependent, although the evolution of the helium core is only calculated for solar element abundances.

The basic equations of chemical evolution are explained in Section 2. Since the explosions of SNe Ia are delayed with respect to SNe II (Greggio & Renzini 1983), the element abundances in metal-poor stars are determined mainly by SNe II. Hence, the adopted standard model for the chemical evolution in the solar neighbourhood can easily explain the enhancement of α-elements in metal-poor stars, assuming that the [Mg/Fe] ratios given by SN II nucleosynthesis are high enough.

5.2 Observational constraints

There are several observational features in the solar neighbourhood, basically constraining different parameters. In the subsections below, we will discuss in detail the influence of the parameters on the abundance distribution function (ADF), the age–metallicity relation (AMR), the current supernova rates, and the element abundances in the Sun. The parameters have to be adjusted to provide the best possible *simultaneous* fit to the existing

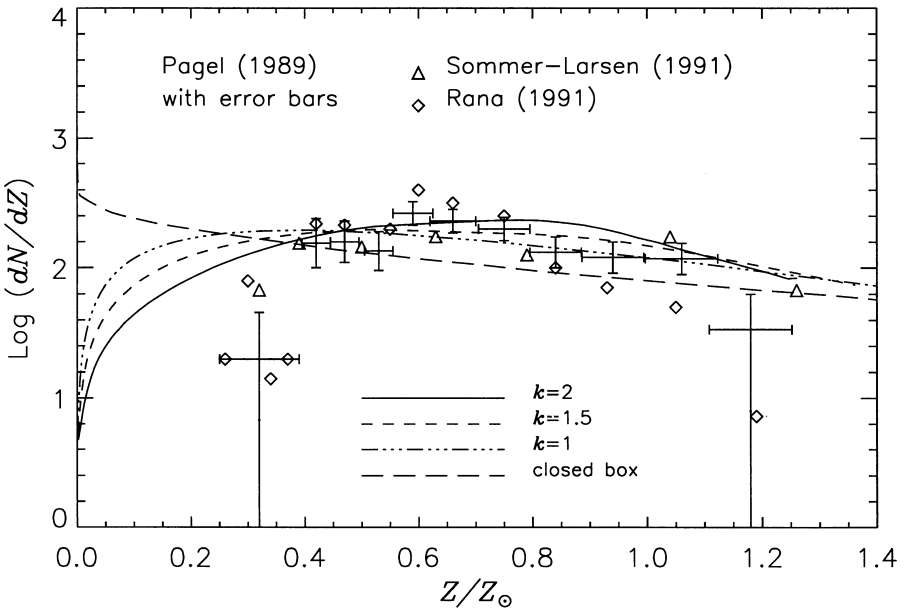

Figure 11. The abundance distribution function (ADF) giving the number of stars that are born per unit metallicity log(dN/dZ) as a function of metallicity. The observational data points with error bars refer to the reanalysis of the Pagel & Patchett data (1975) by Pagel (1989), taking the metallicity-excess calibration of Cameron (1985) into account. Additional re-interpretations of the data set are by Rana (1991) and Sommer-Larson (1991) respectively with correction for the increase of the velocity dispersion with time and for the vertical height distribution of dwarfs. The long-dashed line shows the calculated ADF for a closed box model without infall. While this model definitely fails to match the observations, the models with the inclusion of infall can reproduce at least the general shape of the observed ADF. The best fit refers to the exponent $k = 2$ of the Schmidt law for fixed accretion time-scale $\tau_{\rm disc} = 4$ Gyr. The parameters ν and k are chosen such that the same amount of gas is converted to stellar mass in all models.

observational data. In Table 7 we summarize how the various parameters can be constrained by the different observational features. The right-hand column of the table gives the final adopted values. The calculations are performed using the stellar yields of TNH96. Additional computations for WW95 yields under the same conditions are made in order to work out the influence of stellar nucleosynthesis. The Galactic age is assumed to be $t_{\rm now} = 15$ Gyr (Timmes et al. 1995); the age of the Sun is 4.5 Gyr. The value of the surface density in the solar neighbourhood is assumed to be $77\,{\rm M}_\odot\,{\rm pc}^{-2}$ (Kuijken & Gilmore 1989a,b,c, 1991; Statler 1989; Gould 1990). Stellar lifetimes are taken from Schaller et al. (1992).

5.2.1 *Abundance distribution function*

The differential ADF gives the number of stars that are born per unit metallicity as a function of metallicity. Pagel & Patchett (1975) derived this relation for the solar vicinity (∼25 pc) with a sample of 132 G dwarfs. The most important feature of the ADF is the paucity of extremely metal-poor stars. Assuming a closed box for the chemical evolution, the so called simple model predicts too many metal-poor stars (van den Bergh 1962; Schmidt 1963; Tinsley 1980). This deviation is known as the G dwarf problem. The considerations of pre-enrichment (Truran & Cameron 1971) or infall of material (Larson 1972) help to avoid the formation of low-metallicity stars. The latter possibility is used in the adopted model for the solar neighbourhood, assuming the disc to form due to accretion of primordial gas (see equation 19).

The shape of the resulting theoretical ADF depends basically on dynamical parameters like the accretion time-scale $\tau_{\rm disc}$ and the Schmidt law exponent k (Matteucci & François 1989). Fig. 11 shows the results for different choices of the parameter k. To guarantee that in all computations the same total number of stars is formed, the star formation efficiency ν (see equation 20) is reduced for smaller k. The diagram demonstrates the following.

(i) The inclusion of infall solves the G dwarf problem in the sense that the extremely high amount of metal-poor stars as predicted by the closed box model (long-dashed line) is significantly decreased. The general shape of the ADF, the peak at intermediate metallicities, is reproduced by the model.

(ii) The smaller the exponent k, the more stars of high and low metallicity are formed. Since the ADF predicted by the model is already too flat, $k = 2$ may be the best choice.

A better fit to the ADF data requires an improvement of the adopted model. Since there are both too many metal-poor and too many metal-rich stars, a different description of the infall term may be necessary. In addition, the consideration of pre-enrichment of the infalling gas further reduces the number of low-metallicity stars. Since the aim of this work is to inspect the influence of different stellar yields on the chemical evolution in the solar vicinity in the framework of the standard infall model, we simply use the ADF to constrain the model parameters without improving the model to obtain better fits.

Fig. 12 shows the ADF for different accretion time-scales. For $\tau_{\rm disc} = 3$ and 5 Gyr the numbers of metal-poor and metal-rich stars are overestimated, respectively. Thus, we use $\tau_{\rm disc} = 4$ Gyr in our simulations.

5.2.2 *Age–metallicity relation*

The age–metallicity relation (AMR) shows the ratio [Fe/H] indicating the metallicity as a function of the ages of the stars (Twarog 1980). Since different element abundances of the ISM at different times are locked in stars of different ages, this corresponds to the

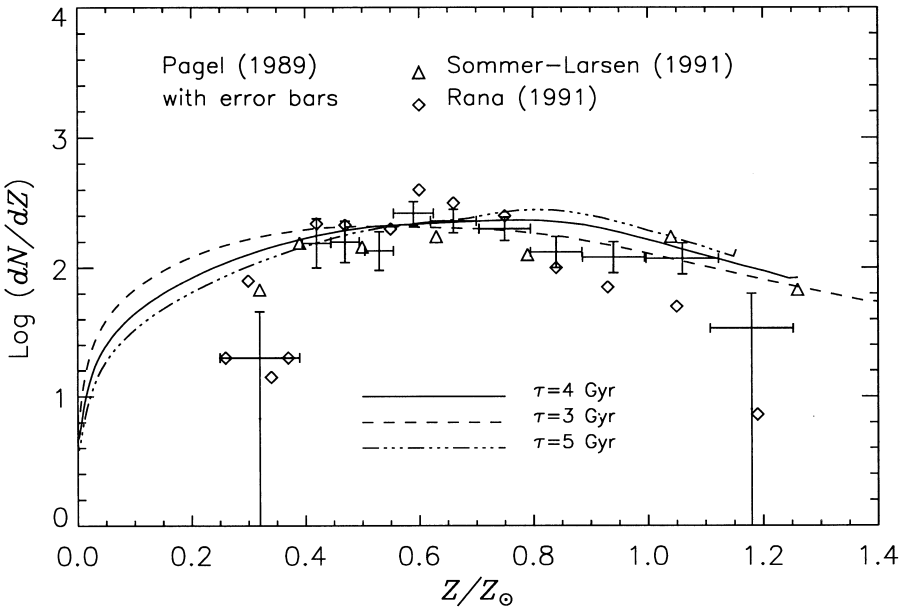

Figure 12. The abundance distribution function (ADF) giving the number of stars that are born per unit metallicity log(dN/dZ) as a function of metallicity. For a short description of the data points see Fig. 11. In this plot, the accretion time-scale is varied. Since a longer accretion time-scale supports the formation of metal-rich stars, the best fit to the data is obtained for $\tau_{\rm disc} = 4$ Gyr. The Schmidt exponent is $k = 2$ as worked out above.

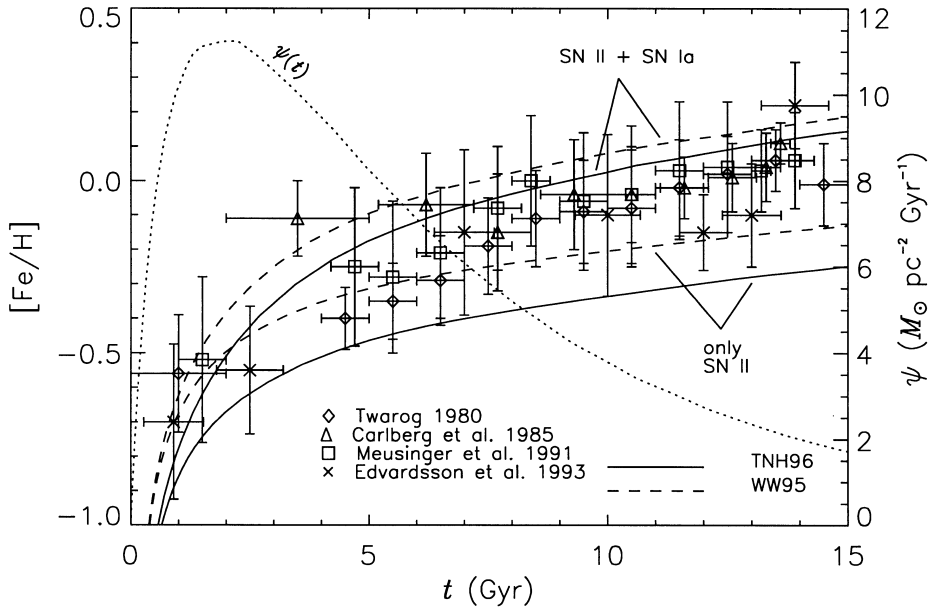

Figure 13. The age–metallicity relation (AMR) for the solar neighbourhood. The symbols indicate the observational data, where as the error bars denote the spread of many stars in the data. Twarog (1980) determined age and metallicity for two samples of 1007 and 2742 local disc stars, respectively. Carlberg et al. (1985) and Meusinger, Reimann & Stecklum (1991) reanalysed these data using new isochrones from VandenBerg (1985). Edvardsson et al. (1993) did not re-examine the Twarog data but derived abundances for 189 F and G disc dwarfs in the solar vicinity. The plot shows that for both SN II nucleosynthesis prescriptions, the enrichment due to SNe Ia is necessary to reproduce the AMR in the solar neighbourhood. A comparison between the solid and the dashed lines [TNH96 and WW95 (model B) SN II yields, respectively] confirms the result from Section 4 that WW95 produce ~0.08 dex more iron. The dotted curve shows the SFR ($M_\odot\,pc^{-2}\,Gyr^{-1}$) as a function of time. The value for today ($t = 15$ Gyr) is in agreement with observations (Güsten & Mezger 1983).

evolution of [Fe/H] in the ISM as a function of time. In the first 2 Gyr of the evolution when the SFR is at its maximum, [Fe/H] rises very steeply to a value of ~ -0.5 dex. The increase flattens out significantly and converges to solar metallicity at $t \approx 10$ Gyr. Fig. 13 shows that this behaviour is well reproduced by the simulations. Star formation (dotted line) is occurring over the whole range of 15 Gyr with a peak of $11\,M_\odot pc^{-2}Gyr^{-1}$ at $t = 1.9$ Gyr. Fitting an exponential law like

$$\psi(t) \sim e^{-t/\tau}$$

to the range $5 - 15$ Gyr where the SFR is decreasing leads to $\tau \approx 8$ Gyr.

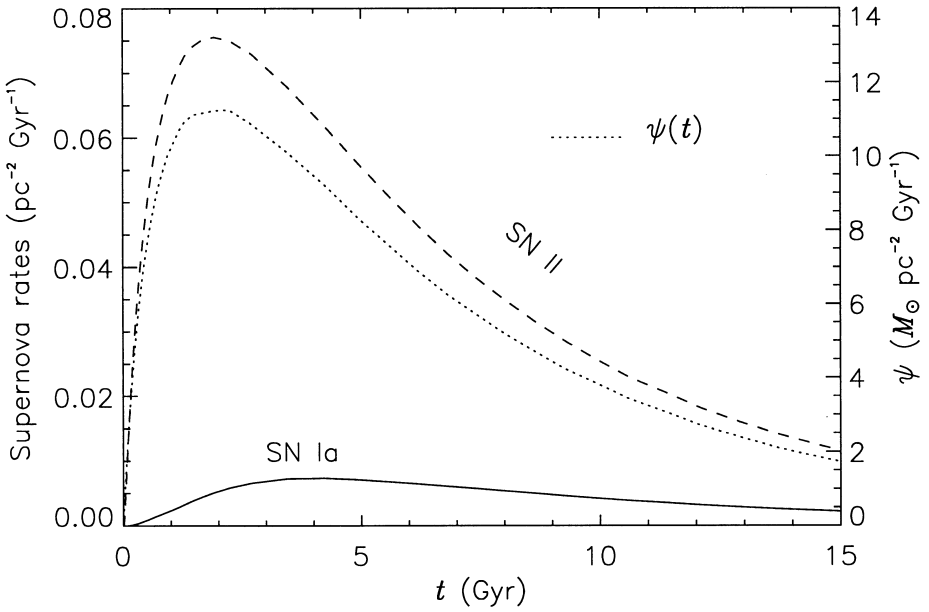

Figure 14. The plot shows the rates of both types of supernovae and the SFR as a function of time. The enrichment due to SNe Ia is delayed with respect to SNe II. The dotted curve demonstrates that the rate of SNe II – occurring in high-mass and short-lived stars – directly depends on the SFR. The calculated number ($pc^{-2}\,Gyr^{-1}$) of SNe II occurring today is in rough agreement with observational estimates (see text). The relative frequency of SNe II to SNe Ia is highly dependent on the parameter A and is in agreement with observations (van den Bergh & Tammann 1991). The fraction A of close binaries has to be chosen to fit the supernova rates and the AMR (Fig. 13) simultaneously.

The iron abundance at large t is significantly determined by the contribution of SNe Ia. The simulations excluding enrichment by SNe Ia clearly underestimate the production of iron.[3] Furthermore, the fraction of iron contributed by the different types of SNe depends on the adopted stellar yields. WW95 models (dashed lines) produce ~0.08 dex more iron than TNH96 (see Section 4). Using TNH96 yields, 60 per cent of the produced iron comes from SNe Ia; according to WW95 models this amount decreases to 50 per cent. Because of the higher iron yield, WW95 models fit the AMR relation worse, but are still within the error bars.

The total amount of iron in the ISM strongly depends on the fraction A of close binary systems. The AMR could be slightly better fitted for a reduced iron production, thus for a lower parameter A. However, this parameter is additionally constrained by the relative frequency of the different types of supernovae.

5.2.3 *Supernova rates*

Unfortunately, the current rates of both types of SNe (Ia and II) in spiral galaxies and in the solar neighbourhood are still uncertain (van den Bergh & Tammann 1991). Since there is no consensus, the range allowed by observations is fairly large. The theoretical relative frequency of SNe II and Ia is mainly determined by the parameter A. In their review paper, van den Bergh & Tammann (1991) claim $N_{\rm SNII}/N_{\rm SNIa} \approx 2.7$ for Sab–Sb galaxies and $N_{\rm SNII}/N_{\rm SNIa} \approx 8$ for Sc–Scd galaxies. Since our Galaxy is assumed to have a Hubble type between Sb and Sc (van den Bergh & Tammann 1991), a relative frequency of $N_{\rm SNII}/N_{\rm SNIa} \approx 5$ seems to be a reasonable estimate. This value is in agreement with our calculations.

Fig. 14 shows the rates of SNe II and Ia as a function of time. While the relative frequency of SNe II and Ia basically constrains the parameter A, the absolute number of SNe II occurring today depends on the parameters ν, k and $\tau_{\rm disc}$, the values of which are already chosen to fit the ADF. Assuming that SNe II occur in stars above 8 $M_\odot$, Tammann (Tammann 1982; van den Bergh & Tammann 1991) estimates a surface density of $N_{\rm SNII} \approx 0.02\,pc^{-2}\,Gyr^{-1}$ in the solar neighbourhood from historical data. However, because of the small size of the sample, this value is quite uncertain. Indeed, van den Bergh (van den Bergh & Tammann 1991) claims that the historical data may overestimate the absolute number of SNe II significantly. Thus, the calculated value of $N_{\rm SNII} \approx 0.01\,pc^{-2}\,Gyr^{-1}$ is still acceptable.

[3]This statement is basically independent of $m_{\rm min}$, since the abundance *ratio* of iron to oxygen is underestimated without SNe Ia.

Table 8. Numerical results of the chemical evolution in the solar neighbourhood compared with observational constraints. The adopted input parameters are given in Table 7. The current fraction of gas $M_{\rm g}/M_{\rm tot}(t_{\rm now})$ is taken from Rana & Basu (1992); the current accretion rate ($M_\odot\,pc^{-2}\,Gyr^{-1}$) comes from observations of high-velocity H I clouds (see Timmes et al. 1995 and references therein). Solar element abundances (by mass) are adopted from Anders & Grevesse (1989) – meteoritic values.

	TNH96	WW95	Observation
$M_{\rm g}/M_{\rm tot}(t_{\rm now})$	0.13	0.13	0.10 ± 0.03
$f(t_{\rm now})$	0.46	0.46	$0.2 - 1.0$
Solar Z	1.96(−2)	1.86(−2)	1.88(−2)
Solar ^{1}H	6.96(−1)	6.89(−1)	7.06(−1)
Solar ^{16}O	9.92(−3)	9.36(−3)	9.59(−3)
Solar ^{24}Mg	4.80(−4)	3.68(−4)	5.15(−4)
Solar ^{56}Fe	1.26(−3)	1.41(−3)	1.17(−3)

5.2.4 *Solar element abundances*

The model assumes that disc formation started 15 Gyr ago. Since the Sun is ~4.5 Gyr old, the element abundances in the ISM predicted by the model have to be solar at $t \approx 10.5$ Gyr.

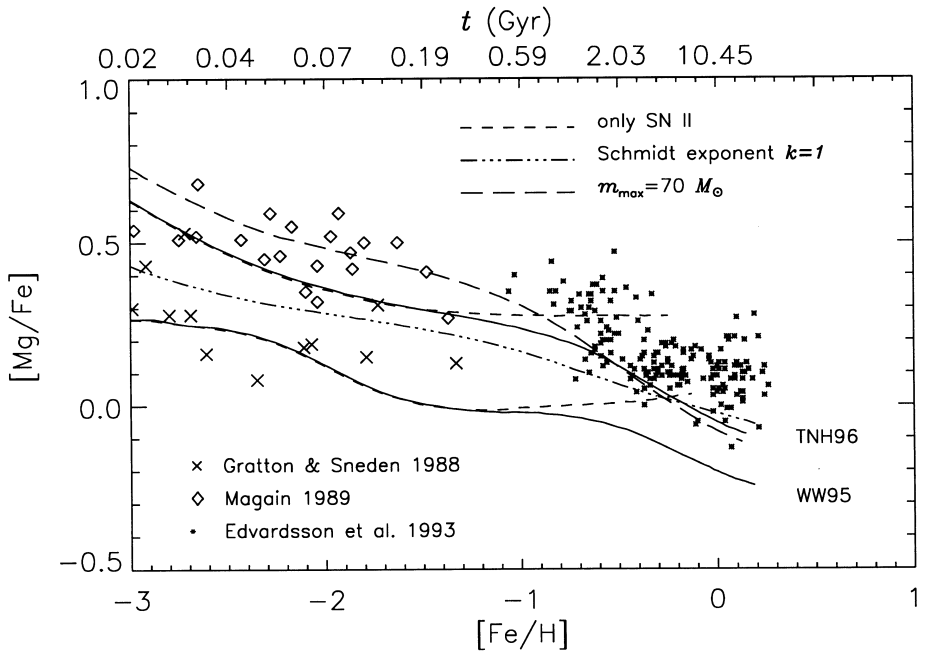

Figure 15. The abundance ratio [Mg/Fe] as a function of [Fe/H] and time (upper x-axis). Magain (1989) derived element abundances in 20 metal-poor halo stars leading to a mean [Mg/Fe] of 0.48 dex. Gratton & Sneden (1988) measured the abundances of 12 metal-poor field giants and derived a mean [Mg/Fe] $\approx$0.27 dex. The two solid lines show the results of the simulations for SN II yields of TNH96 and WW95 (model B), respectively, taking enrichment due to both types of SNe into account. The dashed curve corresponds to calculations only considering SNe II. The abundance ratio reaches the SN II SSP value, once a complete SN II generation of stars enriches the ISM ($m_t \leq 11\,M_\odot$). The value of the 'plateau' is approximately the SSP value of SN II as given in Table B5. At higher metallicities, the iron-dominated ejecta of SNe Ia drive the ratio down. The plot shows that the [Mg/Fe] ratio in the ejecta of WW95 SNe is too low to explain the observational data. The dash–dotted and the long-dashed lines show the results for $k = 1$ and $m_{max} = 70\,M_\odot$, respectively (both TNH96 yields).

In Section 2, we showed how to constrain the SFR (parameters ν and k), the IMF slope (x) and the stellar yield from observational data of the accretion rate, the current gas fraction and the element abundances. The time-scale for disc formation τ_{disc} is constrained by the accretion rate which is observed today (see caption of Table 8).[4] Having fixed $f(t)$ and m_{min}, the current fraction of gaseous mass constrains the mean SFR ($\rightarrow \nu, k$), depending on the IMF slope. We showed that, considering an element with relatively certain yield, the calculated solar abundance of this element depends on $\bar{\psi}$ and x. Thus, τ_{disc}, ν, k and x are fixed.

Fig. 2 shows that WW95 and TNH96 differ only slightly in the calculated oxygen yield. Furthermore, oxygen is mainly produced in massive stars of small stellar lifetimes τ_m, thus the neglect of τ_m in the arguments in Section 2 is valid. Hence, we assume this yield to be the most certain and use oxygen to pin down the IMF slope. Having done this, we can analyse whether the stellar yields of various elements are in agreement with observations. Table 8 shows the comparison between the calculated quantities and their observational constraints. The element abundances of ^{1}H, ^{16}O and Z are best reproduced (due to the above strategy): WW95 and TNH96 differ only marginally; the deviations from observational data are between 1 and 4 per cent. However, in the case of magnesium, the situation is different: the calculated ^{24}Mg abundance deviates from observational data by 7 per cent (TNH96) and 29 per cent (WW95). Reproducing the solar oxygen abundance, the calculated magnesium abundance is too low, especially with WW95 nucleosynthesis. Hence, the predicted ratio between the two element abundances is not in agreement with observations. Since SNe II are the main contributors to the Mg enrichment, we can conclude that the magnesium yield of SNe II is clearly underestimated by WW95.

Although ^{56}Fe also deviates from the observational value, one cannot directly draw conclusions on the iron yield of SNe II, because of the large contribution due to SNe Ia.

5.2.5 *[Mg/Fe]*

We now turn to consider the element abundances observed in stars of various metallicities in the solar neighbourhood, being the last important observational constraint on theoretical models. Gratton & Sneden (1988) and Magain (1989) determined [Mg/Fe] in metal-poor halo stars; Edvardsson et al. (1993) determined [Mg/Fe] in disc stars with [Fe/H]≥ -1. These data together with the theoretical predictions from the model using the parameters of Table 7 are plotted in Fig. 15.

The scatter of the data for [Fe/H]< -1 is extremely large. A reasonable average in the range $-3 \leq$[Fe/H]≤ -1 seems to be $0.3 \leq$[Mg/Fe]≤ 0.4 dex. While TNH96 [Mg/Fe] yields are high enough to fit this value, WW95 fail to reproduce such large values. The same preliminary conclusion was already made in Section 4.

Timmes et al. (1995) also realized that the produced [Mg/Fe] ratio in WW95 is too low to explain the data, and suggested a reduction of the SN II iron yield by a factor of 2. On the other hand, as discussed in Section 4, the iron yields of stellar masses smaller than $20\,M_\odot$ are in good agreement with the observational data from SN1987A and SN1991J. Thus, it is reasonable to halve the iron yield of stellar masses *greater* than $20\,M_\odot$. We showed that this

[4]Today's accretion rate of 0.2–1.0 $M_\odot\,pc^{-2}\,Gyr^{-1}$ estimated from observations of high-velocity H I clouds (see Timmes et al. 1995 and references therein) allows $\tau_{disc} \approx 3$–5.5 Gyr. The more specific value of 4 Gyr is constrained by the ADF.

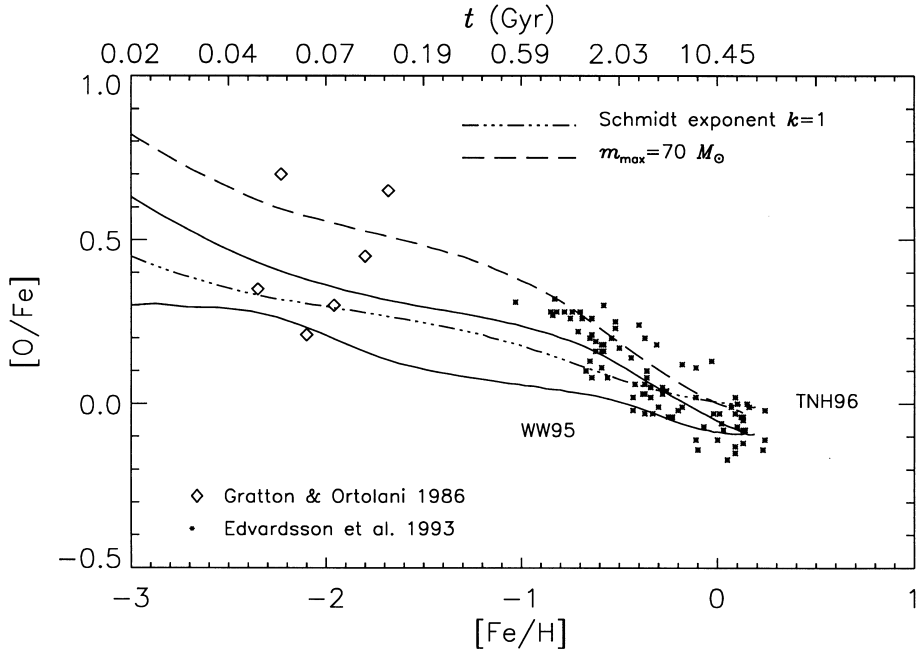

Figure 16. The abundance ratio [O/Fe] as a function of [Fe/H] and time (upper x-axis). The two solid lines show the results of the simulations for SN II yields of TNH96 (upper line) and WW95, respectively. The diagram shows that the [O/Fe] ratio in the solar neighbourhood is well fitted by the model. The dash–dotted and the long-dashed lines show the results for $k = 1$ and $m_{\rm max} = 70\,{\rm M}_\odot$, respectively (both TNH96 yields).

Table 9. As Table 8, considering different upper mass cut-offs for TNH96 nucleosynthesis. In order to maintain the agreement with the discussed observational constraints, the following input parameters had to be re-adjusted: $x = 1.5$, $A = 0.06$, $\nu = 1.1\,{\rm Gyr}^{-1}$.

	$40\,{\rm M}_\odot$	$70\,{\rm M}_\odot$	Observation
$M_{\rm g}/M_{\rm tot}(t_{\rm now})$	0.13	0.13	0.10 ± 0.03
$f(t_{\rm now})$	0.46	0.46	$0.2 - 1.0$
Solar Z	1.96(−2)	1.81(−2)	1.88(−2)
Solar ^{1}H	6.96(−1)	7.17(−1)	7.06(−1)
Solar ^{16}O	9.92(−3)	9.93(−3)	9.59(−3)
Solar ^{24}Mg	4.80(−4)	4.43(−4)	5.15(−4)
Solar ^{56}Fe	1.26(−3)	1.21(−3)	1.17(−3)

results in a shift of 0.08 dex to higher [Mg/Fe] values, which is not enough to explain a [Mg/Fe] overabundance of $0.3 - 0.4$ dex.

Since a flatter IMF would result in an overestimation of the solar metallicity and oxygen abundance, the observed trend can only be produced with an increased Mg yield. Since it is the Mg/O ratio that is underestimated, a variation of $m_{\rm min}$ is not suitable to solve the problem either.

Timmes et al. (1995) claim that a small contribution of SNe Ia or intermediate- and low-mass stars to the magnesium enrichment could solve the problem without increasing the SN II yields, but both alternatives seem to be unlikely, for the following reasons.

(i) Low-mass stars ($1–8\,{\rm M}_\odot$) form CO-white dwarfs and therefore do not burn carbon to magnesium (Renzini & Voli 1981).

(ii) Intermediate-mass stars ($8–11\,{\rm M}_\odot$) may even produce a lower [Mg/Fe] ratio than high-mass stars, because the ratio decreases with decreasing mass (see Fig. 4). If this trend can be approximately extrapolated to lower masses, those stars do not increase the value of [Mg/Fe] in the ISM.

(iii) SNe Ia may be candidates for a higher magnesium production. On the other hand, the [Mg/Fe] ratio is underestimated in a regime at low metallicities where SN II products dominate and SNe Ia do not play any role.

However, uncertainties in convection theory and stellar evolution are high enough to cause different Mg yields of SNe II, which is convincingly demonstrated in the discrepancy between WW95 and TNH96.

The observational data points in Fig. 15 show two different slopes in different metallicity ranges. The progression of [Mg/Fe] is very flat in the low-[Fe/H] region and only slightly decreasing with increasing metallicity. This belongs to the regime in the first 70 Myr (see scale on the upper x-axis), when SNe II are dominating the enrichment of the ISM. For $[{\rm Fe/H}] \gtrsim -1$, SNe Ia enter the game and drive down the [Mg/Fe] ratio because of their iron-dominated ejecta. The decrease of [Mg/Fe] with increasing [Fe/H] becomes notably steeper. Although the theoretical curves reflect this behaviour roughly, using TNH96 yields the slope at low metallicities is still too steep, especially for $-3 \leq [{\rm Fe/H}] \leq -2$.

This decrease becomes flatter for the smaller Schmidt exponent $k = 1$ as indicated by the dash–dotted line. However, while the choice of $k = 1$ may improve the agreement with the data in the [Mg/Fe]–[Fe/H] diagram, the ADF is more badly reproduced (see Fig. 11). The offset to the data of $\sim$0.1 dex seems to have its origin in too low a magnesium yield. Since the model parameters are chosen to reproduce the solar oxygen abundance, it is interesting to consider the [O/Fe] ratio as a function of [Fe/H], too.

5.2.6 [O/Fe]

Again we compare the theoretical results with observations by Edvardsson et al. (1993) at high metallicities and Gratton & Ortolani (1986) in the low-metallicity regime (Fig. 16). These data points are very few and show a large scatter. Thus we

concentrate on the discussion of the Edvardsson et al. data. These are well fitted by the model using TNH96 nucleosynthesis, hence the oxygen abundance in the solar neighbourhood is reproduced as well. The calculation with a lower Schmidt exponent k (TNH96 yields, dash–dotted line) clearly fails to match the observed [O/Fe]. Although WW95 models suffice to produce a solar [O/Fe] ratio, they give a bad fit to the data for [Fe/H] < 0.

5.3 On the upper mass cut-off

As already mentioned, we additionally performed calculations with $m_{\rm max} = 70\,{\rm M}_\odot$ and TNH96 nucleosynthesis. The fitting parameters had to be re-adjusted; the new values and the results for the calculated solar abundances are given in Table 9. Again, the parameters were chosen to match the observational constraints simultaneously.

The solar Mg abundance is even more badly reproduced, since the ratio of magnesium to oxygen decreases with the inclusion of 70-$M_\odot$ stars (see also Table 6). A further remarkable effect is the stronger influence of SNe Ia on the enrichment of iron (parameter A), because iron is the only element (of the considered ones) that is not additionally ejected by extremely high-mass stars. The ratio $N_{\rm SNII}/N_{\rm SNIa} \approx 3$ is still within the range allowed by observation; it may be even a better fit to the historical data (see discussion above).

The effect on the [Mg/Fe]–[Fe/H] diagram is shown by the long-dashed curve in Fig. 15. The ratio [Mg/Fe] is higher by ~0.1 dex in the low-metallicity regime, whereas it is still too small at higher metallicities ($-0.7 \leq$ [Fe/H] ≤ 0.3). The long-dashed line in Fig. 16 shows that the oxygen abundance in the solar neighbourhood can still be reproduced.

The other observational constraints are also matched. The differential ADF changes as if there were a kind of pre-enrichment: it increases more rapidly at the lower Z. However, already at $Z/{\rm Z}_\odot = 0.05$ it presents too many objects, with respect to the observations.

5.4 Delayed mixing

The upper x-axis in Fig. 15 shows that the steep decrease of the TNH96 curve at low metallicities comes from the short time-scales in this regime. On the other hand, this is a consequence from the IMA, assuming that the stellar ejecta mix immediately with the ISM. Although there is no doubt that this assumption is not realistic (Schmidt 1963; Tinsley 1975), most chemical evolution calculations hold this approximation. The validity of the IMA depends on the time-scale of the mixing process. Malinie et al. (1993) claim that, due to chemical inhomogeneities in the disc, re-mixing and star formation may be delayed by 10^{8-9} yr. We will include the consideration of delayed mixing in our calculations and inspect the influence of different mixing time-scales on the observational constraints discussed above.

5.4.1 *The two gas phases*

We distinguish between two different phases of the gas component: the active and the inactive phases. The inactive gas consists of the enriched stellar ejecta. Since this component is hot and not homogeneously distributed, stars cannot form out of this phase. The active phase, instead, is assumed to be cool and well mixed, hence star formation is possible only in the active gas phase. In order to keep the circle of star formation and chemical enrichment alive, the inactive phase converts to the active star-forming phase on a certain time-scale, which includes both the cooling and the mixing processes. The time-scale is treated as a free parameter in the simulations.

To include this scenario in the calculations, we modify the equations (3) and (7) presented in Section 2:

$$\mathrm{d}M_{\rm g}^{\rm inactive}/\mathrm{d}t = E - \frac{1}{\tau_{\rm mix}}\, M_{\rm g}^{\rm inactive}, \tag{21}$$

$$\mathrm{d}M_{\rm g}^{\rm active}/\mathrm{d}t = -\psi + f + \frac{1}{\tau_{\rm mix}}\, M_{\rm g}^{\rm inactive}. \tag{22}$$

To keep the equations as simple as possible, we assume the mass flow between the two gas phases to be proportional to the total amount of inactive gas divided by the mixing time-scale. We now have to distinguish between the abundance in the active gas phase and the abundance in the inactive gas phase:

$$M_{\rm g}^{\rm inactive}\, \mathrm{d}X_i^{\rm inactive}/\mathrm{d}t = E_i - X_i^{\rm inactive}\, E, \tag{23}$$

$$M_{\rm g}^{\rm active}\, \mathrm{d}X_i^{\rm active}/\mathrm{d}t$$

$$= (X_i^{\rm inactive} - X_i^{\rm active})\frac{1}{\tau_{\rm mix}}\, M_{\rm g}^{\rm inactive} + (X_{i,f} - X_i^{\rm active})f. \tag{24}$$

The SFR described by the Schmidt law is then dependent on the density of the active gas:

$$\psi = \nu M_{\rm tot}\left[\frac{M_g^{\rm active}}{M_{\rm tot}}\right]^k. \tag{25}$$

The infalling material is assumed to mix instantaneously with the active gas.

5.4.2 *Observational constraints*

We now show the influence of the different mixing time-scales on the observational constraints discussed in the previous subsections. The values of the parameters in Table 7 are not changed.

5.4.2.1 [Mg/Fe] in metal-poor stars. Fig. 17 shows the results for mixing time-scales of 0.01, 0.1 and 1 Gyr in the [Mg/Fe]–[Fe/H] diagram. Since the delay due to the mixing processes elongates the time-scales (see upper x-axis for the case $\tau_{\rm mix} = 0.1$ Gyr), the curve becomes flatter. The effect is at maximum at early epochs and becomes negligible at solar ages.

The figure additionally shows the results for the inclusion of the enrichment due to 70-$M_\odot$ stars and delayed mixing (TNH96 yields, $\tau_{\rm mix} = 0.1$ Gyr, long-dashed line).

5.4.2.2 AMR. While the fit to the data in the [Mg/Fe]–[Fe/H] diagram has become better, the constraint on the AMR relation is still fulfilled. Even the results for mixing time-scales of the order of 10^9 Gyr are still in agreement with observations.

5.4.2.3 Solar element abundances. Table 10 gives the element abundances in both gas phases for different mixing time-scales. Since the Sun forms out of active gas at $t = 10.45$ Gyr, these abundances have to match the solar values given by observation (Table 8). The abundances in the inactive gas are systematically higher. The numbers show that the abundances of the elements H, O and Z are well reproduced for the same set of parameters as given in Table 7, especially for $\tau_{\rm mix} \leq 0.1$ Gyr.

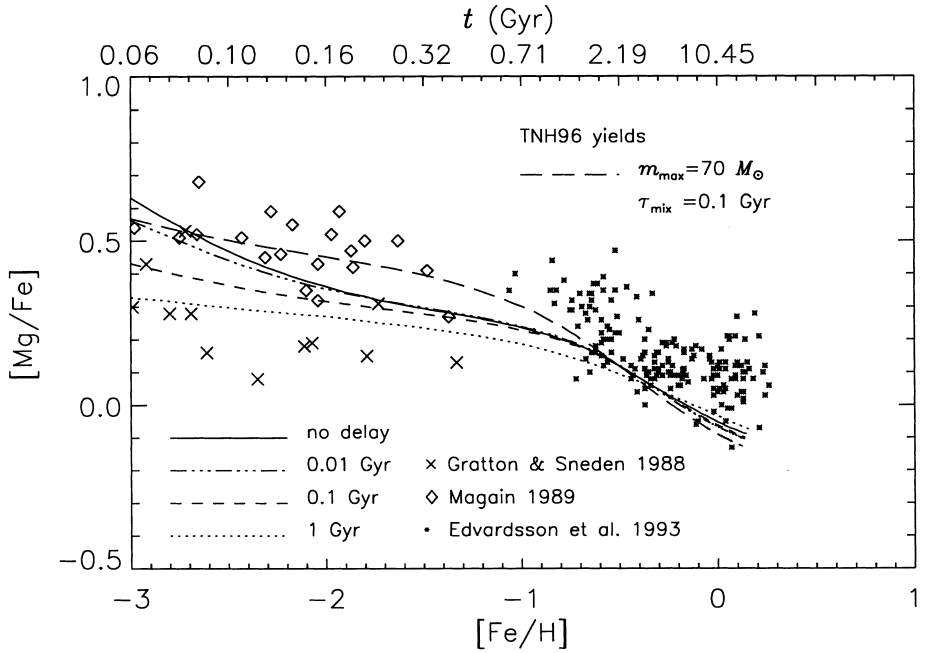

Figure 17. The abundance ratio [Mg/Fe] as a function of [Fe/H]. For a detailed description see the caption of Fig. 15. In these calculations, we relax the assumption of the IMA and consider different time-scales for the mixing of the stellar ejecta with the ISM. SN II yields of TNH96 are used. The upper x-axis gives the progression of time for the case $\tau_{\rm mix} = 0.1$ Gyr. The more the mixing is delayed, the flatter the curve becomes. The approximately constant value (there might be a slight decrease) of [Mg/Fe] in metal-poor stars in the range $-3 \leq$ [Mg/Fe] ≤ -1 can be better reproduced when a delay in the mixing is assumed. The long-dashed line shows the result for $m_{\rm max} = 70\,{\rm M}_\odot$ and $\tau_{\rm mix} = 0.1$ Gyr.

Table 10. As table 8 for the two different gas phases and various mixing time-scales. Stellar yields are taken from TNH96. The gas fractions give the fractions of active and inactive gas in the total mass at $t = 15$ Gyr. The element abundances of the active and inactive gas phases are given for $t = 10.45$ Gyr (birth of the Sun). For a comparison with solar element abundances, the active gas phase has to be considered. The abundances in the inactive gas are systematically higher.

$\tau_{\rm mix}$	0.01 Gyr	0.1 Gyr	1 Gyr
$M_{\rm g}^{\rm active}/M_{\rm tot}(t_{\rm now})$	1.30(−1)	1.30(−1)	1.35(−1)
$M_{\rm g}^{\rm inactive}/M_{\rm tot}(t_{\rm now})$	6.55(−5)	6.70(−4)	8.38(−3)
$Z^{\rm active}$	1.88(−2)	1.91(−2)	2.08(−2)
$Z^{\rm inactive}$	5.70(−2)	5.73(−2)	5.85(−2)
$\rm H^{active}$	6.98(−1)	6.97(−1)	6.92(−1)
$\rm H^{inactive}$	5.70(−1)	5.70(−1)	5.67(−1)
$\rm O^{active}$	9.43(−3)	9.58(−3)	1.05(−2)
$\rm O^{inactive}$	2.86(−2)	2.88(−2)	2.96(−2)
$\rm Mg^{active}$	4.57(−4)	4.64(−4)	5.17(−4)
$\rm Mg^{inactive}$	1.34(−3)	1.35(−3)	1.41(−3)
$\rm Fe^{active}$	1.23(−3)	1.25(−3)	1.32(−3)
$\rm Fe^{inactive}$	3.93(−3)	3.93(−3)	3.87(−3)

Since, for a larger delay in the mixing, at the end less gas is formed into stars, the fractions of both gas phases increase. However, more metal-poor stars are formed in the beginning. As a consequence, the element abundances at $t \gg \tau_{\rm mix}$ (i.e. when the Sun is born) become higher with increasing $\tau_{\rm mix}$. At $t \approx \tau_{\rm mix}$, instead, a larger delay causes lower abundances in the ISM. For the case of the iron abundance, this pattern is demonstrated in Fig. 18.

5.4.2.4 ADF. The formation of more low-metallicity stars, though, has consequences for the derived ADF. The discussion in Section 5.2.1 showed that the adopted infall model cannot fit the ADF in the whole metallicity range. At both ends of low and high metallicity, too many stars are formed. Certainly, the inclusion of delayed mixing worsens the situation. Fig. 19 shows the results for the different mixing time-scales.

There is no doubt that the consideration of delayed mixing processes in the disc gives a more realistic approach to the chemical evolution in the solar neighbourhood (Schmidt 1963; Tinsley 1975). Since the formation of more metal-poor stars can hardly be avoided with a delayed mixing, the additional consideration of pre-enrichment of the disc due to early halo evolution (Burkert, Truran & Hensler 1992) is necessary to solve the G dwarf problem. However, to treat this scenario properly, more sophisticated evolution models, calculating halo and disc evolution separately, have to be considered.

6 CONCLUSIONS

Using two different sets of models for SN II yields (WW95 and TNH96), we have analysed the influence of stellar nucleosynthesis on the chemical evolution of galaxies, in particular the element abundances in the solar neighbourhood.

It turns out that there is a good agreement in the SN II yields of oxygen and total metallicity between WW95 and TNH96 over the whole mass range of SNe II. However, from the point of view of galactic chemical evolution, there are significant differences in the magnesium yields in the mass range $18 - 25\,{\rm M}_\odot$. For a 20-$\rm M_\odot$ star, the Mg yield calculated by TNH96 is ∼5 times higher than the result of WW95. We have shown that, since the IMF is giving more

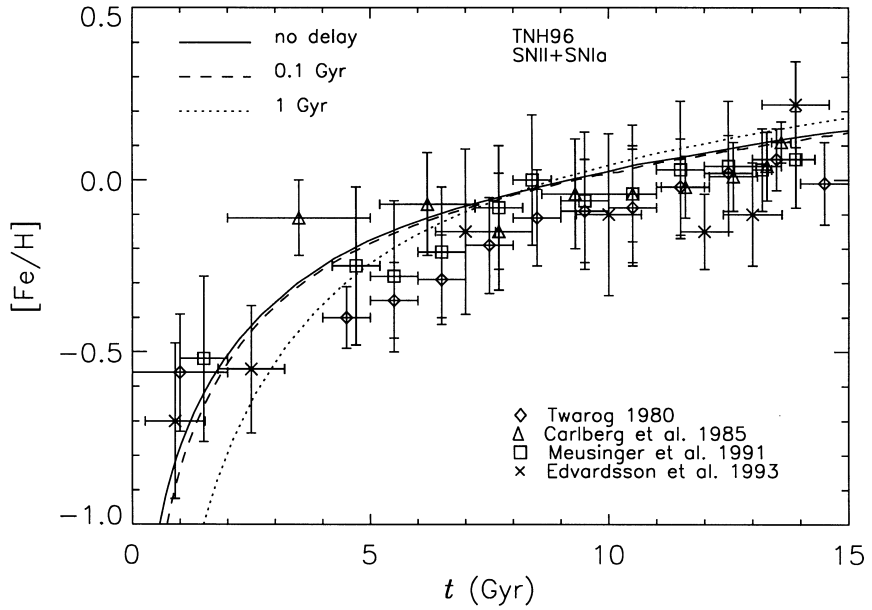

Figure 18. The age–metallicity relation (AMR) for the solar neighbourhood. For a detailed description see Fig. 13. The different lines show the influence of the different mixing time-scales on the AMR relation. For time-scales of the order of 0.1 Gyr, the delayed mixing only affects the results at small t. In particular, the reproduction of the solar element abundances at $t = 10.45$ Gyr is not violated.

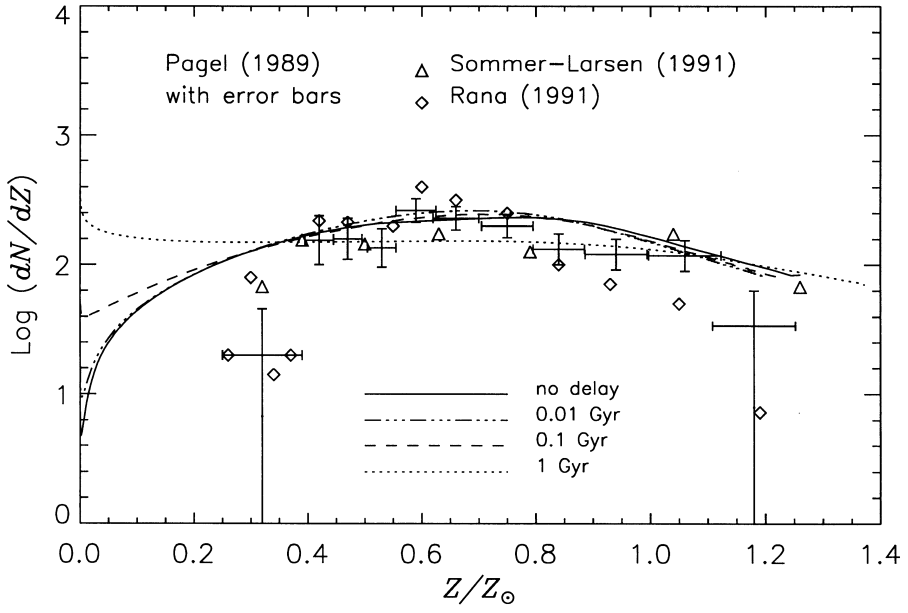

Figure 19. The abundance distribution function (ADF) giving the number of stars that are born per unit metallicity log(dN/dZ) as a function of metallicity. For a detailed description see Fig. 11. The set of parameters is given in Table 8. The different linestyles show the results for different mixing time-scales. The larger the delay in the mixing processes, the more metal-poor stars form. The agreement with the observational data becomes worse. The consideration of pre-enrichment may be necessary.

weight to smaller masses, the results of chemical evolution models are very sensitive to this discrepancy. The iron yield, instead, is mainly uncertain in the upper mass range. WW95 and TNH96 agree very well in the lower mass range ($13 \leq m \leq 20\,\mathrm{M}_{\odot}$) which is well constrained by the observed light curves of SN II events (SN1987A, SN1991J). However, in high-mass stars with $m \geq 25\,\mathrm{M}_{\odot}$, WW95 models give significantly higher Fe yields than TNH96. In total, this leads to lower [Mg/Fe] ratios produced by WW95 nucleosynthesis. A significantly super-solar value is only reached in high-mass stars (Fig. 4) which are dominating the enrichment in the first few 10^7 yr of chemical evolution.

Only 0.04 Gyr after the birth of the first stars, the complete generation of SN II exploding stars in the mass range $8 - 40\,\mathrm{M}_{\odot}$ is enriching the ISM. We have calculated the SN II SSP yields of O, Mg and Fe for different IMF slopes and both nucleosynthesis prescriptions. The result is that TNH96 nucleosynthesis leads to

[Mg/Fe] = 0.26 dex for the Salpeter IMF, while the ratio with WW95 ($Z_\odot$, model B) is 0.05 dex. We have shown that this discrepancy is due to a lower Mg SSP yield of 0.13 dex and a higher Fe SSP yield of 0.08 dex in WW95. Even for a flat IMF with $x = 0.7$, the SSP value of [Mg/Fe] is 0.12 dex with WW95 yields. Without any impact from complex evolution models, from these numbers one can already conclude that the [Mg/Fe] overabundance in both ellipticals and the solar neighbourhood cannot be explained with the stellar yields of the WW95 models.

Applying the standard infall model (Matteucci & Greggio 1986; Timmes et al. 1995; Yoshii et al. 1996) to the chemical evolution of the solar neighbourhood confirms the conclusions drawn from the discussion of the SSP yields. Both the [Mg/Fe] overabundance in metal-poor stars and the magnesium abundance of the Sun can be better reproduced with the Mg yields of TNH96. In addition to this, we have discussed the relaxation of the instantaneous mixing approximation for the chemical evolution in the solar neighbourhood. For this purpose, we modified the basic equations of chemical evolution separating the gaseous component into two different gas phases. While the inactive phase is enriched by the stellar ejecta, stars can only form out of the active, well-mixed phase. A mass flow from the inactive to the active gas phase on a variable time-scale represents the mixing process. For different mixing time-scales of the order of 10^7, 10^8 and 10^9 yr, we have investigated the influence of a delayed mixing on the reproduction of the observational features. It turns out that a delay in the mixing supports the approximately constant value of [Mg/Fe] in the [Mg/Fe]–[Fe/H] diagram in the low-metallicity range, while the agreement with the age–metallicity relation (AMR) and solar element abundances is not violated. However, since a delayed mixing causes the formation of more low-metallicity stars, the abundance distribution function (ADF) is less well reproduced. On the other hand, the instantaneous mixing of the stellar ejecta is certainly an unrealistic assumption, and the inclusion of a delay is a necessary step to improve chemical evolution models. Hence, the solution of the G dwarf problem in the solar neighbourhood may require a combination of infall and pre-enrichment.

Since TNH96 include the 70-$M_\odot$ star in their computations, we have additionally investigated the influence of a variation of the upper mass cut-off on the theoretical SSP yields and on the chemical evolution in the solar neighbourhood. Applying TNH96 nucleosynthesis, the [Mg/Fe] ratio in the ejecta of one SSP is significantly increased. This result is highly uncertain, however, because TNH96 do not consider fallback, which may play an important role for the nucleosynthetic contribution from high-mass stars. Indeed, extrapolating the results of WW95 to $70\,M_\odot$ leaves the SSP yields basically unchanged. The problem of the underestimation of the solar magnesium abundance remains the same also for TNH96 yields, since the Mg/O ratio in stars more massive than $40\,M_\odot$ is even smaller. However, it is important to investigate quantitatively the metal contribution of stars more massive than $40\,M_\odot$, since they could play an important role in chemical evolution.

In general, we have demonstrated the sensitivity of galactic chemical evolution to nucleosynthesis prescriptions of Type II supernovae. Different stellar yields can significantly alter conclusions on the parameters of chemical evolution models like IMF slope or star formation time-scales. As long as the stellar nucleosynthesis of important elements like magnesium and iron is affected by so many uncertainties, the results from simulations of chemical evolution have to be interpreted by considering the whole range of up-to-date nucleosynthesis calculations.

ACKNOWLEDGMENTS

We thank B. Pagel, the referee of the paper, for carefully reading the first version and giving important comments on the subject. He especially motivated us to explore the influence of the upper mass cut-off on the results of the calculations. We also thank F.-K. Thielemann for useful and interesting discussions. The SFB 375 of the DFG and the Alexander von Humboldt Stiftung (LG) are acknowledged for support.

REFERENCES

Anders E., Grevesse N., 1989, Geochim. Cosmochim. Acta, 53, 197
Arnett W. D., Thielemann F.-K., 1985, ApJ, 295, 589
Arnett W. D., Bahcall J. N., Kirshner R. P., Woosley S. E., 1989, ARA&A, 27, 629
Axer M., Fuhrmann K., Gehren T., 1994, A&A, 291, 895
Axer M., Fuhrmann K., Gehren T., 1995, A&A, 300, 751
Baron E., Hauschildt P. H., Young T. R., 1995, Phys. Rep., 256, 23
Burkert A., Truran J. W., Hensler G., 1992, ApJ, 391, 651
Cameron L. M., 1985, A&A, 146, 59
Carlberg R. G., Dawson P. C., Hsu T., VandenBerg D. A., 1985, ApJ, 294, 674
Caughlan G. R., Fowler W. A., 1988, At. Data Nucl. Data Tables, 40, 283
Caughlan G. R., Fowler W. A., Harris M. J., Zimmermann G. E., 1985, At. Data Nucl. Data Tables, 32, 197
Davies R. E., Sadler E. M., Peletier R. F., 1993, MNRAS, 262, 650
Edvardsson B., Andersen J., Gustafsson B., Lambert D. L., Nissen P. E., Tomkin J., 1993, A&A, 275, 101
Fuhrmann K., Axer M., Gehren T., 1995, A&A, 301, 492
Gehren T., 1995, in Hippelein H., Meisenheimer K., Röser H.-J., eds, Galaxies in the Young Universe. Springer, Heidelberg, p. 190
Gibson B. K., 1997, MNRAS, 290, 471
Gibson B. K., Loewenstein M., Mushotzky R. F., 1997, MNRAS, 290, 623
Gould A., 1990, MNRAS, 244, 25
Gould A., Bahcall J. N., Flynn C., 1997, ApJ, 482, 913
Gratton R. G., Ortolani S., 1986, A&A, 169, 201
Gratton R. G., Sneden C., 1988, A&A, 204, 193
Greggio L., 1997, MNRAS, 285, 151
Greggio L., Renzini A., 1983, A&A, 118, 217
Güsten R., Mezger P. G., 1983, Vistas Astron., 26, 3
Hansen C. J., Wheeler J. C., 1969, Ap&SS, 36, 464
Hashimoto M., Iwamoto K., Nomoto K., 1993a, ApJ, 414, L105
Hashimoto M., Nomoto K., Tsujimoto T., Thielemann F.-K., 1993b, in Käppeler F., ed., Nuclei in the Cosmos II. IOP Publishing, Bristol, p. 587
Hensler G., Burkert A., 1990, Ap&SS, 170, 231
Kroupa P., Tout C. A., Gilmore G., 1993, MNRAS, 262, 545
Kuijken K., Gilmore G., 1989a, MNRAS, 239, 571
Kuijken K., Gilmore G., 1989b, MNRAS, 239, 605
Kuijken K., Gilmore G., 1989c, MNRAS, 239, 651
Kuijken K., Gilmore G., 1991, ApJ, 367, L9
Larson R. B., 1972, Nature Phys. Sci., 236, 7
McWilliam A., Rich R. M., 1994, ApJS, 91, 749
Magain P., 1989, A&A, 209, 211
Malinie G., Hartmann D. H., Clayton D. D., Mathews G. J., 1993, ApJ, 413, 633
Matteucci F., 1994, A&A, 288, 57
Matteucci F., François P., 1989, MNRAS, 239, 885
Matteucci F., Greggio L., 1986, A&A, 154, 279
Matteucci F., Franco J., François P., Treyer M.-A., 1989, Rev. Mex. Astron. Astrofis., 18, 145
Mehlert D., Saglia R. P., Bender R., Wegner G., 1998, A&A, in press
Meusinger H., Reimann H.-G., Stecklum B., 1991, A&A, 245, 57

Nomoto K., 1980a, in Wheeler J. C., ed., Type I Supernovae. Univ. of Texas, Austin, p. 164
Nomoto K., 1980b, Space Sci. Rev., 27, 563
Nomoto K., 1981, in Sugimoto D., Lamb D. Q., Schramm D. N., ed., Proc. IAU Symp. 93, Fundamental Problems in the Theory of Stellar Evolution. Reidel, Dordrecht, p. 295
Nomoto K., Hashimoto M., 1988, Phys. Rep., 163, 13
Nomoto K., Thielemann F.-K., Yokoi K., 1984, ApJ, 286, 644
Nomoto K., Iwamoto K., Suzuki T., 1995, Phys. Rep., 256, 173
Nomoto K., Hashimoto M., Tsujimoto F.-K., Kishimoto N., Kubo Y., Nakasato N., 1997, Nucl. Phys. A, 616, 79c
Pagel B. E. J., 1989, in Beckman J. E., Pagel B. E. J., eds, Evolutionary Phenomena in Galaxies. Cambridge Univ. Press, Cambridge, p. 201
Pagel B. E. J., Patchett B. E., 1975, MNRAS, 172, 13
Pagel B. E. J., Tautvaisiene G., 1995, MNRAS, 276, 505
Peletier R., 1989, PhD thesis, Rijksuniversiteit Groningen
Rana N. C., 1991, ARA&A, 29, 129
Rana N. C., Basu S., 1992, A&A, 265, 499
Renzini A., Voli M., 1981, A&A, 94, 175
Salpeter E. E., 1955, ApJ, 121, 161
Scalo J. M., 1986, Fundam. Cosmic Phys., 11, 1
Schaller G., Schaerer D., Meynet G., Maeder A., 1992, A&AS, 96, 269
Schmidt M., 1959, ApJ, 129, 243
Schmidt M., 1963, ApJ, 137, 758
Sommer-Larsen J., 1991, MNRAS, 249, 368
Statler T. S., 1989, ApJ, 344, 217
Sugimoto D., Nomoto K., 1980, Space Sci. Rev., 25, 155
Tammann G. A., 1982, in Rees M., Stoneham R., eds, Supernovae: a Survey of Current Research. D. Reidel, Cambridge, p. 371
Thielemann F.-K., Nomoto K., Hashimoto M., 1996, ApJ, 460, 408 (TNH96)
Timmes F. X., Woosley S. E., Weaver T. A., 1995, ApJS, 98, 617
Tinsley B. M., 1975, ApJ, 197, 159
Tinsley B. M., 1980, Fundam. Cosmic Phys., 5, 287
Tosi M., 1988, A&A, 197, 47
Truran J. W., Burkert A., 1993, in Hensler G., Theis C., Gallagher J., eds, Panchromatic View of Galaxies. Editions Frontieres, Kiel, p. 389
Truran J. W., Cameron A. G. W., 1971, Ap&SS, 14, 179
Tsujimoto T., Nomoto K., Yoshii Y., Hashimoto M., Yanagida S., Thielemann F.-K., 1995, MNRAS, 277, 945
Twarog B. A., 1980, ApJ, 242, 242
van den Bergh S., 1962, AJ, 62, 711
van den Bergh S., Tammann G. A., 1991, ARA&A, 29, 363
VandenBerg D. A., 1985, ApJS, 58, 711
Weaver T. A., Woosley S. E., 1980, in Ehlers J., ed., Texas Conference on Relativistic Astrophysics. Ann. NY Acad. Sci., p. 366
Weaver T. A., Woosley S. E., 1993, Phys. Rep., 227, 65
Weiss A., Peletier R. F., Matteucci F., 1995, A&A, 296, 73
Whelan J., Iben I., Jr, 1973, ApJ, 186, 1007
Woosley S. E., 1986, in Hauck B., Maeder A., eds, Nucleosynthsis and Chemical Evolution. Geneva Observatory, Geneva, p. 1
Woosley S. E., Weaver T. A., 1995, ApJS, 101, 181 (WW95)
Worthey G., Faber S. M., Gonzalez J. J., 1992, ApJ, 398, 69
Yoshii Y., Tsujimoto T., Nomoto K., 1996, ApJ, 462, 266

APPENDIX A: IMF WEIGHTED YIELDS

The figures show the relative contribution of a 1-$M_\odot$ mass interval to the total SN II yields of the elements oxygen, magnesium and iron, and metallicity for different IMF slopes and nucleosynthesis prescriptions (WW95, TNH96). The three models for different explosion energies (A, B and C)[5] and four different initial metallicities ($10^{-4}\,Z_\odot$, $0.01\,Z_\odot$, $0.1\,Z_\odot$ and $Z_\odot$) in WW95 are considered. Each figure shows the results for one particular element and one specified WW95 model (A, B or C). The four panels of each figure show the results for the four different IMF slopes. The four different initial metallicities of WW95 and TNH96 yields are plotted together in each panel. The meanings of the linestyles and symbols are specified in Fig. 1. The quantity dQ_{im}/dm is determined according to equation (17). It is normalized such that the integration over the total mass range of SNe II ($11 - 40\,M_\odot$) is equal to 1. The x-axis give the initial stellar mass on the main sequence. To obtain the fractional contribution of a mass interval, one has to multiply the width of the interval ($M_\odot$) by the mean value of dQ_{im}/dm in this mass range.

[5]See also Table 2.

A1 OXYGEN

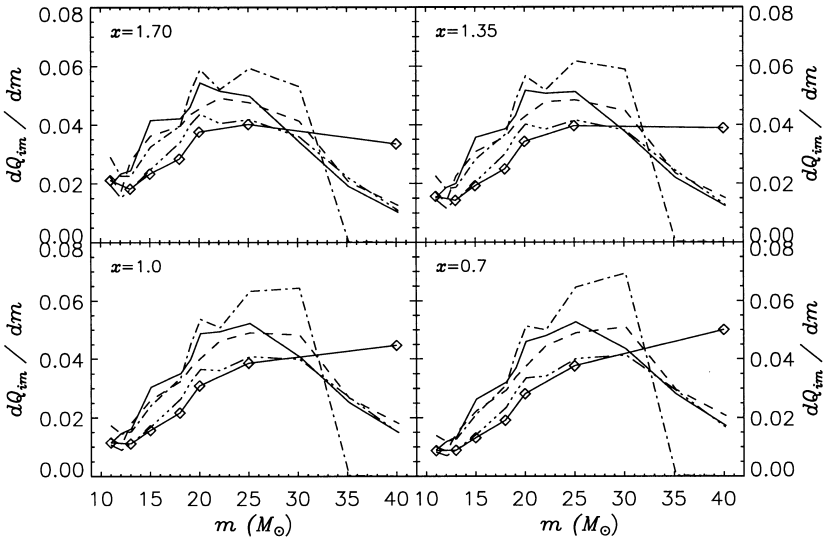

Figure A1. Oxygen: model A.

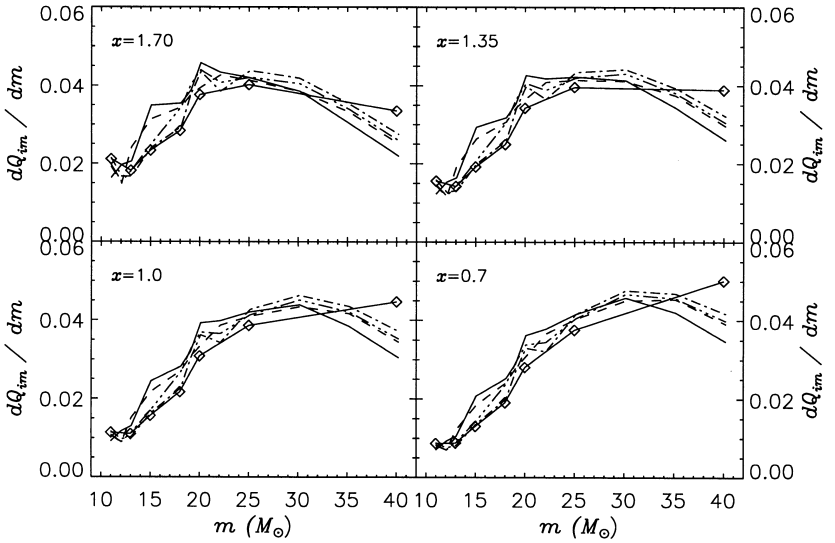

Figure A2. Oxygen: model B.

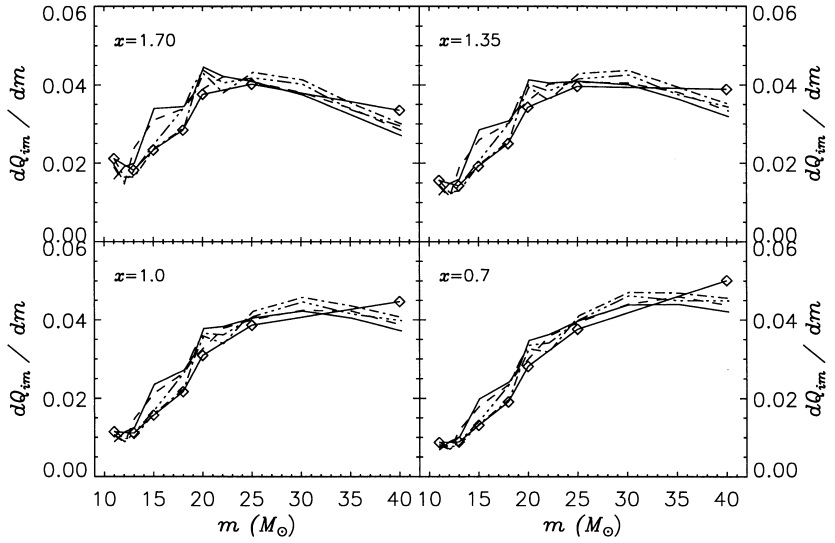

Figure A3. Oxygen: model C.

A2 METALLICITY

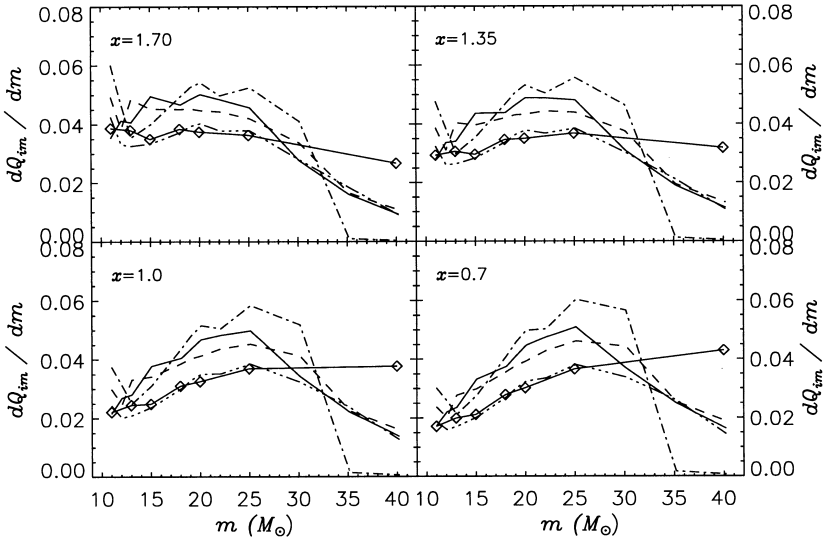

Figure A4. Metallicity: model A.

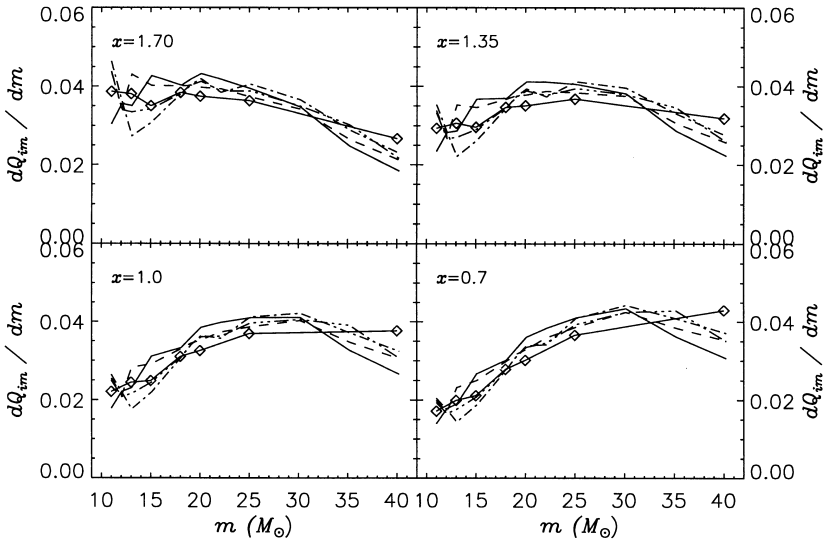

Figure A5. Metallicity: model B.

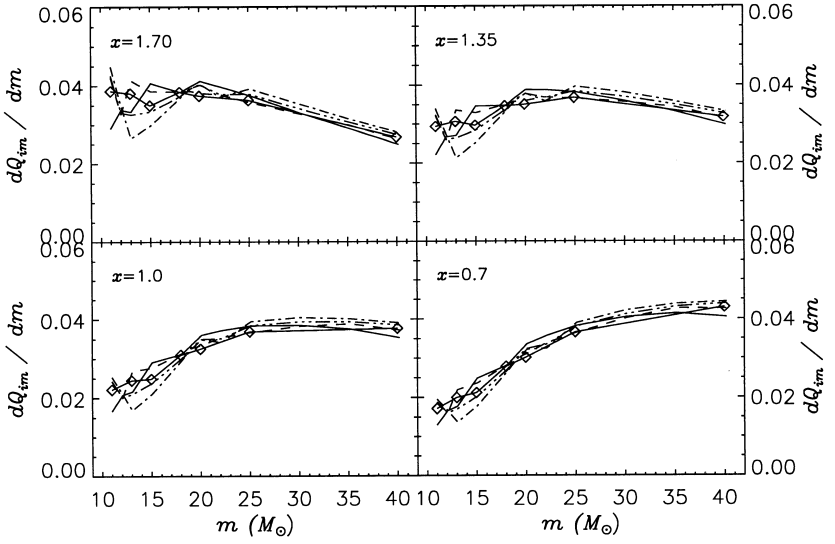

Figure A6. Metallicity: model C.

A3 MAGNESIUM

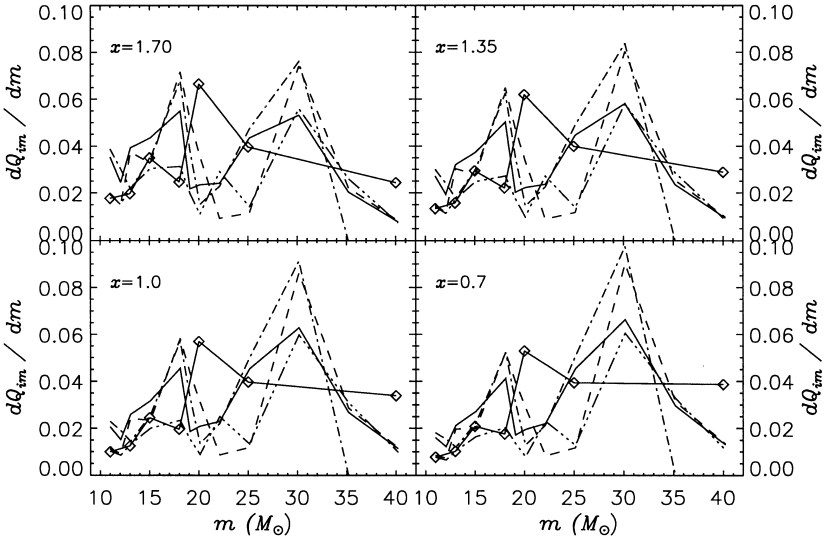

Figure A7. Magnesium: model A.

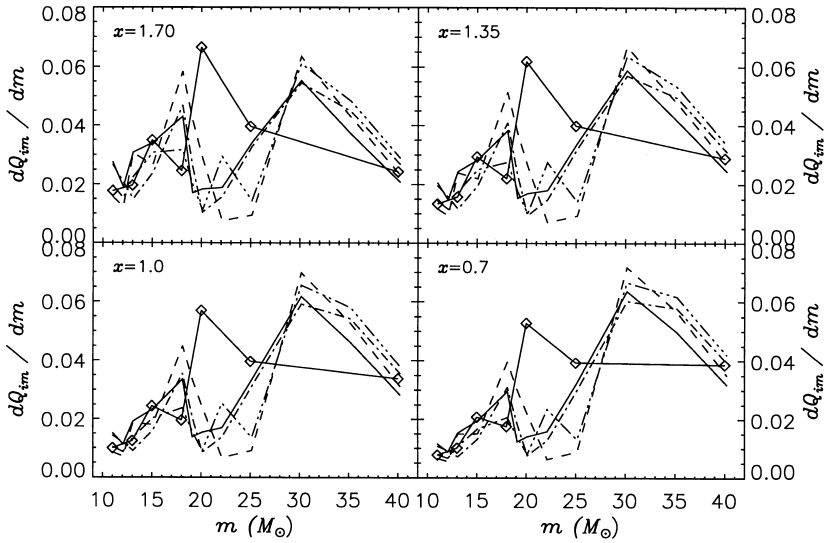

Figure A8. Magnesium: model B.

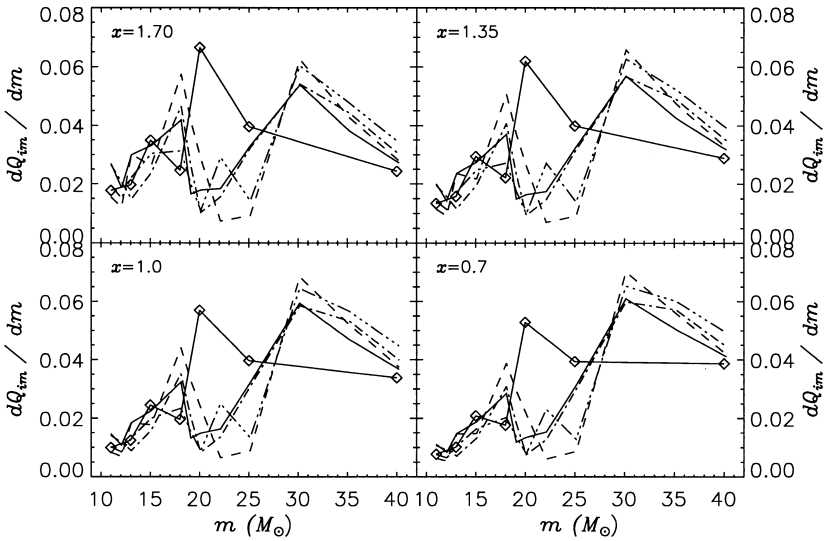

Figure A9. Magnesium: model C.

A4 IRON

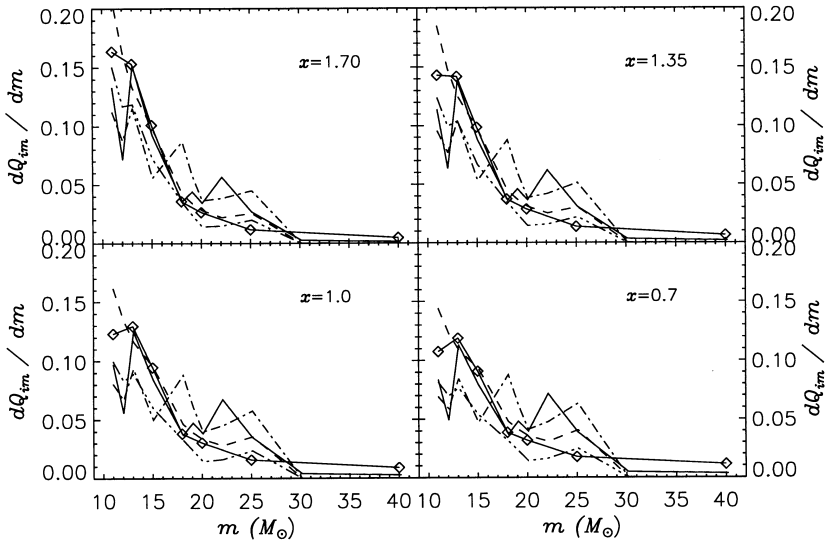

Figure A10. Iron: model A.

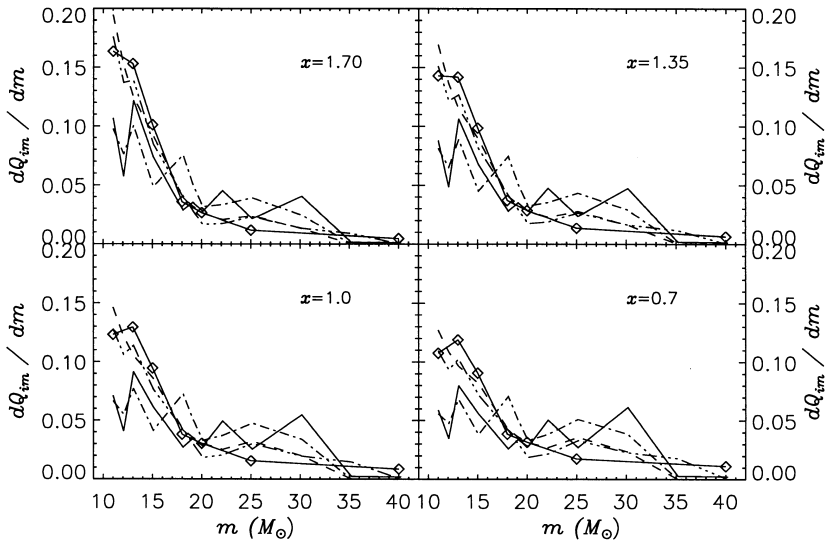

Figure A11. Iron: model B.

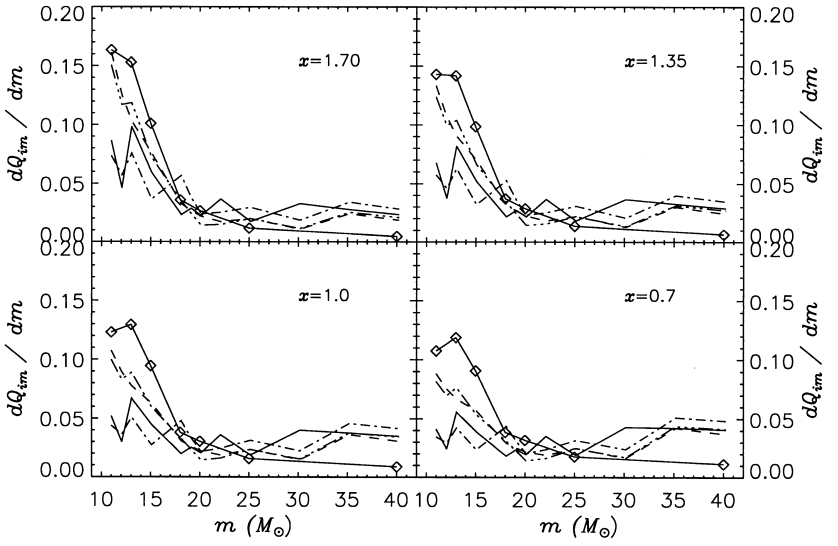

Figure A12. Iron: model C.

APPENDIX B: SSP YIELDS

Tables B1 to B12 to show the abundances of oxygen, magnesium and iron in the ejecta of one generation of SN II exploding stars (SSP yields). Each table refers to a certain IMF slope and explosion model of WW95 (A, B or C). The values are normalized on (meteoritic) solar abundances from Anders & Grevesse (1989) and expressed on a logarithmic scale.

B1 $x = 1.7$

Table B1. WW95 model: A. IMF: $x = 1.70$.

	TNH96	WW95 ($0\,Z_\odot$)	WW95 ($10^{-4}\,Z_\odot$)	WW95 ($0.01\,Z_\odot$)	WW95 ($0.1\,Z_\odot$)	WW95 ($Z_\odot$)
[O]	0.85	0.04	0.61	0.72	0.73	0.76
[Mg]	0.85	0.12	0.52	0.56	0.64	0.60
[Fe]	0.65	0.52	0.51	0.71	0.76	0.61
[O/Fe]	0.19	−0.48	0.10	0.00	−0.03	0.15
[Mg/Fe]	0.19	−0.40	0.01	−0.15	−0.12	−0.01

Table B2. WW95 model: B. IMF: $x = 1.70$.

	TNH96	WW95 ($0\,Z_\odot$)	WW95 ($10^{-4}\,Z_\odot$)	WW95 ($0.01\,Z_\odot$)	WW95 ($0.1\,Z_\odot$)	WW95 ($Z_\odot$)
[O]	0.85	0.43	0.75	0.77	0.79	0.83
[Mg]	0.85	0.44	0.68	0.65	0.73	0.71
[Fe]	0.65	0.68	0.57	0.76	0.79	0.70
[O/Fe]	0.19	−0.26	0.17	0.01	0.00	0.13
[Mg/Fe]	0.19	−0.25	0.11	−0.11	−0.06	0.00

Table B3. WW95 model: C. IMF: $x = 1.70$.

	TNH96	WW95 ($0\,Z_\odot$)	WW95 ($10^{-4}\,Z_\odot$)	WW95 ($0.01\,Z_\odot$)	WW95 ($0.1\,Z_\odot$)	WW95 ($Z_\odot$)
[O]	0.85	0.66	0.75	0.78	0.80	0.85
[Mg]	0.85	0.63	0.69	0.66	0.73	0.72
[Fe]	0.65	0.78	0.70	0.83	0.87	0.80
[O/Fe]	0.19	−0.12	0.06	−0.06	−0.07	0.05
[Mg/Fe]	0.19	−0.15	−0.01	−0.17	−0.14	−0.08

B 2 $x = 1.35$

Table B4. WW95 model: A. IMF: $x = 1.35$.

	TNH96	WW95 ($0\,Z_\odot$)	WW95 ($10^{-4}\,Z_\odot$)	WW95 ($0.01\,Z_\odot$)	WW95 ($0.1\,Z_\odot$)	WW95 ($Z_\odot$)
[O]	0.92	0.05	0.66	0.78	0.79	0.81
[Mg]	0.91	0.13	0.57	0.63	0.69	0.66
[Fe]	0.65	0.50	0.52	0.70	0.75	0.62
[O/Fe]	0.26	−0.45	0.14	0.07	0.04	0.20
[Mg/Fe]	0.26	−0.37	0.05	−0.08	−0.05	0.04

Table B5. WW95 model: B. IMF: $x = 1.35$.

	TNH96	WW95 ($0\,Z_\odot$)	WW95 ($10^{-4}\,Z_\odot$)	WW95 ($0.01\,Z_\odot$)	WW95 ($0.1\,Z_\odot$)	WW95 ($Z_\odot$)
[O]	0.92	0.49	0.82	0.84	0.86	0.90
[Mg]	0.91	0.49	0.76	0.73	0.80	0.78
[Fe]	0.65	0.70	0.59	0.77	0.79	0.73
[O/Fe]	0.26	−0.21	0.22	0.07	0.07	0.17
[Mg/Fe]	0.26	−0.21	0.16	−0.04	0.01	0.05

Table B6. WW95 model: C. IMF: $x = 1.35$.

	TNH96	WW95 ($0\,Z_\odot$)	WW95 ($10^{-4}\,Z_\odot$)	WW95 ($0.01\,Z_\odot$)	WW95 ($0.1\,Z_\odot$)	WW95 ($Z_\odot$)
[O]	0.92	0.74	0.82	0.84	0.86	0.91
[Mg]	0.91	0.70	0.76	0.74	0.80	0.79
[Fe]	0.65	0.82	0.74	0.86	0.89	0.84
[O/Fe]	0.26	−0.08	0.08	−0.01	−0.03	0.07
[Mg/Fe]	0.26	−0.12	0.02	−0.12	−0.09	−0.05

B 3 $x = 1.0$

Table B7. WW95 model: A. IMF: $x = 1.00$.

	TNH96	WW95 ($0\,Z_\odot$)	WW95 ($10^{-4}\,Z_\odot$)	WW95 ($0.01\,Z_\odot$)	WW95 ($0.1\,Z_\odot$)	WW95 ($Z_\odot$)
[O]	0.98	0.07	0.71	0.83	0.84	0.86
[Mg]	0.97	0.13	0.62	0.69	0.75	0.71
[Fe]	0.65	0.47	0.53	0.69	0.74	0.62
[O/Fe]	0.33	−0.41	0.18	0.14	0.10	0.24
[Mg/Fe]	0.32	−0.35	0.09	0.00	0.01	0.09

Table B8. WW95 model: B. IMF: $x = 1.00$.

	TNH96	WW95 ($0\,Z_\odot$)	WW95 ($10^{-4}\,Z_\odot$)	WW95 ($0.01\,Z_\odot$)	WW95 ($0.1\,Z_\odot$)	WW95 ($Z_\odot$)
[O]	0.98	0.55	0.88	0.90	0.92	0.95
[Mg]	0.97	0.54	0.82	0.80	0.86	0.84
[Fe]	0.65	0.71	0.61	0.77	0.78	0.75
[O/Fe]	0.33	−0.16	0.27	0.13	0.13	0.20
[Mg/Fe]	0.32	−0.17	0.21	0.03	0.08	0.09

Table B9. WW95 model: C. IMF: $x = 1.00$.

	TNH96	WW95 ($0\,Z_\odot$)	WW95 ($10^{-4}\,Z_\odot$)	WW95 ($0.01\,Z_\odot$)	WW95 ($0.1\,Z_\odot$)	WW95 ($Z_\odot$)
[O]	0.98	0.81	0.89	0.91	0.92	0.97
[Mg]	0.97	0.77	0.83	0.81	0.87	0.85
[Fe]	0.65	0.86	0.79	0.88	0.91	0.89
[O/Fe]	0.33	−0.05	0.10	0.03	0.01	0.08
[Mg/Fe]	0.32	−0.09	0.04	−0.07	−0.04	−0.03

B 4 $x = 0.7$

Table B10. WW95 model: A. IMF: $x = 0.70$.

	TNH96	WW95 ($0\,Z_\odot$)	WW95 ($10^{-4}\,Z_\odot$)	WW95 ($0.01\,Z_\odot$)	WW95 ($0.1\,Z_\odot$)	WW95 ($Z_\odot$)
[O]	1.03	0.07	0.74	0.87	0.88	0.89
[Mg]	1.01	0.12	0.65	0.73	0.79	0.74
[Fe]	0.64	0.45	0.52	0.67	0.72	0.61
[O/Fe]	0.39	−0.38	0.21	0.20	0.16	0.28
[Mg/Fe]	0.37	−0.32	0.13	0.06	0.07	0.13

Table B11. WW95 model: B. IMF: $x = 0.70$.

	TNH96	WW95 ($0\,Z_\odot$)	WW95 ($10^{-4}\,Z_\odot$)	WW95 ($0.01\,Z_\odot$)	WW95 ($0.1\,Z_\odot$)	WW95 ($Z_\odot$)
[O]	1.03	0.60	0.93	0.95	0.96	1.00
[Mg]	1.01	0.58	0.88	0.86	0.91	0.89
[Fe]	0.64	0.72	0.62	0.77	0.77	0.76
[O/Fe]	0.39	−0.12	0.31	0.18	0.19	0.23
[Mg/Fe]	0.37	−0.14	0.26	0.09	0.14	0.12

Table B12. WW95 model: C. IMF: $x = 0.70$.

	TNH96	WW95 ($0\,Z_\odot$)	WW95 ($10^{-4}\,Z_\odot$)	WW95 ($0.01\,Z_\odot$)	WW95 ($0.1\,Z_\odot$)	WW95 ($Z_\odot$)
[O]	1.03	0.87	0.94	0.95	0.97	1.02
[Mg]	1.01	0.82	0.88	0.86	0.92	0.90
[Fe]	0.64	0.89	0.83	0.90	0.93	0.92
[O/Fe]	0.39	−0.02	0.11	0.05	0.04	0.10
[Mg/Fe]	0.37	−0.07	0.06	−0.04	−0.01	−0.01

This paper has been typeset from a T_EX/L^AT_EX file prepared by the author.